ZFOURGE: Using Composite Spectral Energy Distributions
to Characterize Galaxy Populations at $1 < z < 4$[*]

Ben Forrest[1] , Kim-Vy H. Tran[1,2,3] , Adam Broussard[4], Jonathan H. Cohn[1] , Robert C. Kennicutt, Jr.[5], Casey Papovich[1] ,
Rebecca Allen[3,6] , Michael Cowley[3,7] , Karl Glazebrook[6] , Glenn G. Kacprzak[6] , Lalitwadee Kawinwanichakij[1,11] ,
Themiya Nanayakkara[8] , Brett Salmon[9] , Lee R. Spitler[3,7] , and Caroline M. S. Straatman[10]

[1] George P. and Cynthia W. Mitchell Institute for Fundamental Physics and Astronomy, Department of Physics and Astronomy,
Texas A&M University, College Station, TX 77843, USA; bforrest@physics.tamu.edu
[2] School of Physics, University of New South Wales, Kensington, Australia
[3] Australian Astronomical Observatory, P.O. Box 915, North Ryde, NSW 1670, Australia
[4] Department of Physics and Astronomy, Rutgers, The State University of New Jersey, 136 Frelinghuysen Road, Piscataway, NJ 08854, USA
[5] Steward Observatory, University of Arizona, 933 N. Cherry Avenue, Tucson, AZ 85721-0065, USA
[6] Centre for Astrophysics and Supercomputing, Swinburne University, Hawthorn, VIC 3122, Australia
[7] Department of Physics & Astronomy, Macquarie University, Sydney, NSW 2109, Australia
[8] Leiden Observatory, Niels Bohrweg 2, 2333 CA, Leiden, The Netherlands
[9] Space Telescope Science Institute, Baltimore, MD 21218, USA
[10] Sterrenkundig Observatorium, Universiteit Gent, Krijgslaan 281 S9, B-9000 Gent, Belgium

Abstract

We investigate the properties of galaxies as they shut off star formation over the 4 billion years surrounding peak cosmic star formation. To do this, we categorize $\sim$7000 galaxies from $1 < z < 4$ into 90 groups based on the shape of their spectral energy distributions (SEDs) and build composite SEDs with $R \sim 50$ resolution. These composite SEDs show a variety of spectral shapes and also show trends in parameters such as color, mass, star formation rate, and emission-line equivalent width. Using emission-line equivalent widths and strength of the 4000 Å break, $D(4000)$, we categorize the composite SEDs into five classes: extreme emission line, star-forming, transitioning, post-starburst, and quiescent galaxies. The transitioning population of galaxies shows modest Hα emission (EW$_{REST} \sim 40$ Å) compared to more typical star-forming composite SEDs at $\log_{10}(M/M_\odot) \sim 10.5$ (EW$_{REST} \sim 80$ Å). Together with their smaller sizes (3 kpc vs. 4 kpc) and higher Sérsic indices (2.7 vs. 1.5), this indicates that morphological changes initiate before the cessation of star formation. The transitional group shows a strong increase of over 1 dex in number density from $z \sim 3$ to $z \sim 1$, similar to the growth in the quiescent population, while post-starburst galaxies become rarer at $z \lesssim 1.5$. We calculate average quenching timescales of 1.6 Gyr at $z \sim 1.5$ and 0.9 Gyr at $z \sim 2.5$ and conclude that a fast-quenching mechanism producing post-starbursts dominated the quenching of galaxies at early times, while a slower process has become more common since $z \sim 2$.

Key words: galaxies: evolution – galaxies: high-redshift

1. Introduction

Since the beginning of the millennium, the number of galaxies with multiwavelength photometric observations and accurate redshifts has exploded. A wide range of surveys, including the Deep Lens Survey (Wittman et al. 2002), Sloan Digital Sky Survey (Abazajian et al. 2003), imaging in the Hawaii Hubble Deep Field North (Capak et al. 2004), the Newfirm Medium Band Survey (NMBS; van Dokkum et al. 2009), 3D-*HST* (van Dokkum et al. 2011), the Cosmic Assembly Near-Infrared Deep Extragalactic Legacy Survey (CANDELS; Koekemoer et al. 2011), and the FourStar Galaxy Evolution Survey (ZFOURGE; Straatman et al. 2016) have increased our knowledge of galaxy formation and evolution tremendously. With upcoming facilities such as the Large Synoptic Survey Telescope (LSST), we will soon truly be in an era where analyzing each individual galaxy will be prohibitive. As such, we must find automated ways to study large numbers of galaxies. One approach is to group galaxies together based on common spectral characteristics—optimizing this

methodology will be an important piece of understanding the life cycles of galaxies through cosmic time.

Previous studies have grouped galaxies together in a variety of ways. Often galaxies with similar values of a given parameter, e.g., mass, star formation rate (SFR), Sérsic index, radius, rest-frame color, emission-line strength, or infrared (IR) luminosity, will be analyzed together, and all such categorizations can tease out important pieces of information (e.g., Shapley et al. 2003; Brinchmann et al. 2008; Nakajima & Ouchi 2014; Eales et al. 2017, 2018). Perhaps most prevalent in extragalactic studies, plotting the rest-frame colors (U–V) and (V–J) against one another has been used to classify galaxies into star-forming or quiescent regimes, approximate dust content, and constrain galaxy evolution (e.g., Labbé et al. 2005; Wuyts et al. 2007; Williams et al. 2009; Brammer et al. 2011; Whitaker et al. 2011; Patel et al. 2012; Papovich et al. 2015). More recently, other trends in this *UVJ* diagram have been noticed for high-redshift populations, such as increasing specific SFR (sSFR) perpendicular to the quiescent wedge (see Figure 26 of Straatman et al. 2016; Fang et al. 2018).

More statistically robust methods have also been used for grouping galaxies, as early as in Miller & Coe (1996) with the use of self-organizing maps. More recent methods have

---

included local linear embedding (Vanderplas & Connolly 2009), principal components analysis (PCA; Wild et al. 2014; Maltby et al. 2016; Rowlands et al. 2018), and composite spectral energy distribution (SED) construction (Kriek et al. 2011; Kriek & Conroy 2013; Forrest et al. 2016, 2017). For the latter, using medium-band and broadband filters to construct composite SEDs allows for impressive sensitivity and sample size. At the same time, this method enables analysis of emission lines and discriminates more clearly between stellar populations than is typically possible without spectroscopic data.

In this work, we use spectral diagnostics calculated from composite SEDs to categorize galaxies and show that this classification scheme accurately picks out rare populations, as supported by other properties and scaling relations. This includes galaxies with strong nebular emission lines (emission-line galaxies [ELGs]), as well as galaxies transitioning from star-forming to quiescent regimes, which we split into two groups—transition galaxies (TGs), which show Hα emission, and post-starburst galaxies (PSBs), which do not show Hα emission.

PSBs have been a historically rare population and have been studied in small numbers for some time (e.g., Couch & Sharples 1987; Tran et al. 2003, 2004; Poggianti et al. 2009). Such galaxies have recently undergone a period of strong star formation, which has stopped within the past several hundred million years. As a result, their spectra are dominated by main-sequence A stars with significant Balmer absorption (e.g., Dressler & Gunn 1983). While analysis of these galaxies allows insight into the mechanisms by which galaxies cease forming stars, such galaxies generally require spectroscopic confirmation, further preventing large samples from being found, particularly at higher redshifts. Additionally, it is not clear that all galaxies undergo such a phase, as the mechanisms behind the quenching of galaxies are still uncertain and may vary (Tran et al. 2003; Wilkinson et al. 2017).

The timescale for which galaxies remain in this post-starburst state is thought to be on the order of 10^8 yr (e.g., Wild et al. 2016) and may be dependent on environment (e.g., Tran et al. 2003, 2004; Poggianti et al. 2009). As this timescale is relatively short, finding such galaxies is somewhat challenging, and several methods have been used to more easily identify these objects. Whitaker et al. (2012b) use *UVJ* selection and single stellar population models, while other recent works such as Wild et al. (2014, 2016) have used PCA for identifying PSBs from multiwavelength photometry alone. Spectroscopic follow-up of these objects (Maltby et al. 2016) has shown a high success rate for this method.

Alternative pathways to quenching are also suggested by the population of non-PSB galaxies in what has come to be called the "green valley" introduced in Martin et al. (2007), Salim et al. (2007), Schiminovich et al. (2007), and Wyder et al. (2007)—in this work we use the term TGs. Originally selected to be between the star-forming sequence and quenched population of the color–magnitude diagram, similar galaxies have since been selected based on relations between colors, stellar masses, stellar mass surface densities, and SFRs (e.g., Mendez et al. 2011; Fang et al. 2013; Schawinski et al. 2014; Pandya et al. 2017). Studies have hypothesized different quenching routes that galaxies may take before shutting off star formation permanently, including the idea of rejuvenation, in which a galaxy stops and restarts star formation multiple times

(e.g., Darvish et al. 2016; Davé et al. 2017; Nelson et al. 2018; Pandya et al. 2017). Here we use composite SEDs to infer quenching timescales of galaxies over the 4 billion years around peak cosmic star formation.

This paper builds on the composite SED work published in Forrest et al. (2016, 2017). Here we reconstruct composite SEDs using the full ZFOURGE sample (previous work used a subset of the full data set) and provide a more detailed description of our data and methodology in Sections 2 and 3, respectively. Section 4 relays our measurements based on the composite SEDs, as well as parameters from the individual galaxies themselves. We then present our composite SEDs in terms of spectral features from the composite SEDs and analysis of the photometry of individual galaxies (Sections 5 and 6). Discussion of the TGs (Section 7) and conclusions (Section 8) follow. The entire set of composite SEDs and associated parameters are presented in the Appendix. Throughout the work we assume a cosmology with $H_0 = 70 \, \mathrm{km \, s^{-1} \, Mpc^{-1}}$, $\Omega_m = 0.3$, and $\Omega_\Lambda = 0.7$ and make use of the AB magnitude system.

2. Data

We use multiwavelength photometry from the FourStar Galaxy Evolution Survey (ZFOURGE; Straatman et al. 2016) in our work. This survey obtained deep near-IR imaging with the FourStar imager (Persson et al. 2013) of three legacy fields: CDFS (Giacconi et al. 2002), COSMOS (Scoville et al. 2007), and UDS (Lawrence et al. 2007). Straatman et al. (2016) combined *K*-band imaging data from a number of surveys (Retzlaff et al. 2010; Hsieh et al. 2012; McCracken et al. 2012; Fontana et al. 2014; Almaini et al. 2017) to create deep mosaics used as the detection images for the ZFOURGE catalogs (see Section 2.3 of Straatman et al. 2016, for details). Morphological data for ZFOURGE galaxies cross-matched with *Hubble Space Telescope* (*HST*)/WFC3/F160W CANDELS data from van der Wel et al. (2012) are also included.

In addition to these data, multiwavelength data from a variety of sources were included in a set of publicly released catalogs (Giavalisco et al. 2004; Erben et al. 2005; Hildebrandt et al. 2006; Taniguchi et al. 2007; Furusawa et al. 2008; Wuyts et al. 2008; Erben et al. 2009; Hildebrandt et al. 2009; Nonino et al. 2009; Cardamone et al. 2010; Grogin et al. 2011; Koekemoer et al. 2011; Windhorst et al. 2011; Brammer et al. 2012). The CDFS, COSMOS, and UDS fields have 40, 37, and 26 filter bandpass observations ranging from 0.3 to 8 μm with 80% completeness limits of 26.0, 25.5, and 25.8 AB mag in the stacked K_s band, respectively (Straatman et al. 2016). These catalogs are particularly well suited to the composite SED method owing to their accurate photometric redshifts (1%–2%; Nanayakkara et al. 2016), broad range of rest-frame wavelengths probed, and deep imaging, which allows for inclusion of faint galaxies at high redshifts.

SFRs are from publicly available catalogs compiled by Tomczak et al. (2016), which used legacy UV data, as well as data from *Spitzer*/MIPS (GOODS-S: PI Dickinson; COSMOS: PI Scoville; UDS: PI Dunlop) and *Herschel*/PACS (GOODS-S: Elbaz et al. 2011; COSMOS and UDS: PI Dickinson). Active galactic nucleus (AGN) host catalogs from Cowley et al. (2016) are also provided in the ZFOURGE data release.

3. Composite SED Construction

3.1. Sample Selection

The construction of composite SEDs requires grouping galaxies together based on SED shape, as determined from multiwavelength photometry. This method is based on the work presented in Kriek et al. (2011), with minor changes made in Forrest et al. (2016, 2017).

We begin by selecting a sample over some redshift range, based on Easy and Accurate z_{phot} from Yale (EAZY; Brammer et al. 2008) outputs included in the ZFOURGE catalogs (Straatman et al. 2016). EAZY fits linear combinations of sets of input galaxy spectral templates to photometry, allowing calculation of photometric redshifts and rest-frame colors. Combined with the medium bands of ZFOURGE, this yields precise photometric redshifts, which are necessary to minimize scatter in the resulting composite SEDs.

The strength of the composite SED method is only realized when different redshifts are used. Grouping galaxies over a narrow redshift range does not improve sampling of the rest-frame wavelengths over observations of an individual galaxy. Therefore, it is important that the redshift range of galaxies being considered is broad enough to enable continuous spectral coverage via deredshifted photometry. Kriek et al. (2011) used a redshift range of $0.5 < z < 2.0$, Forrest et al. (2016) required $1.0 < z < 3.0$, and Forrest et al. (2017) was based on composite SEDs from galaxies in the range $2.5 < z < 4.0$. The overlap in redshift ranges was to increase the sample size in the Forrest et al. (2017) work. We regenerate composite SEDs from the latter two redshift ranges using the publicly released set of ZFOURGE catalogs.

The signal-to-noise cut for our selection is $S/N_{K_s} > 20$. In general, this limits the galaxies in the sample to those that have well-defined SEDs through accurate photometry. Combined with the similarity index described below, this ensures that two identical galaxies with observations different only as a result of noise determined by our S/N cut will be grouped together. Finally, we eliminate stars and other contaminants by requiring the catalog flag use = 1, and we remove X-ray-selected, IR-selected, and radio-selected AGN hosts as identified in Cowley et al. (2016). These cuts produce 7351 galaxies in $1 < z < 3$ and 1294 galaxies in $2.5 < z < 4$.

3.2. Grouping Method

Once we have our sample, we run each galaxy through EAZY, using nine templates from Fioc & Rocca-Volmerange (1999), Brammer et al. (2008), Erb et al. (2010), and Whitaker et al. (2011) as shown in Figure 1. These templates and the K_s luminosity prior used are described in Section 5.1 of Straatman et al. (2016). Using these best fits, we generate synthetic photometric points in 22 rest-frame filters for every galaxy. These rest-frame filters have their center points at wavelengths $\log_{10}(\lambda_{c,i}/\mathring{A}) = 3.13 + 0.073i$, are symmetric around those points in $\log_{10}$ space, are equivalent in width in $\log_{10}$ space, and have responses of unity between their bounds. Thus, they weight every wavelength of those between $1226 < \lambda/\mathring{A} < 49580$ equally in $\log_{10}$ space.

Between any two galaxies, we only compare those filters that lie between the rest-frame wavelengths photometrically observed for both galaxies. Thus, galaxies at vastly different redshifts will have fewer filters compared—this is taken into account when choosing a sample redshift range. The rest-frame
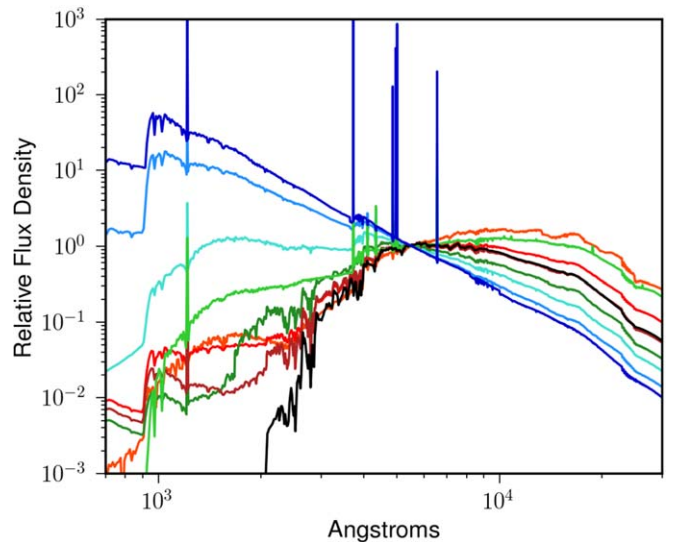

Figure 1. EAZY templates used to fit galaxy SEDs, the same as used in Straatman et al. (2016). The template with the greatest flux at 1000 Å is a high-EW model from Erb et al. (2010), while the template with the greatest flux at 1 μm is an old, dusty template. Other templates are included with EAZY (Brammer et al. 2008).

synthetic photometry, f_λ^{rf}, is used to obtain a metric describing the similarity of any two galaxies as in Kriek et al. (2011):

$$b_{12} = \sqrt{\frac{\Sigma(f_\lambda^{rf1} - a_{12}f_\lambda^{rf2})^2}{\Sigma(f_\lambda^{rf1})^2}} \qquad (1)$$

$$a_{12} = \frac{\Sigma f_\lambda^{rf1} f_\lambda^{rf2}}{\Sigma(f_\lambda^{rf2})^2}. \qquad (2)$$

Here b measures the difference between the shapes of two galaxies' SED fits, while a is a scaling factor to account for flux differences. If two galaxies have $b < 0.05$, we consider them to be *analogs*.

After calculating this b-parameter for combinations of all galaxies that passed our cuts, we look for the galaxy with the largest number of analogs, which we term the *primary*. We then take the primary and its analogs out of our list of galaxies and set them aside. This process is repeated until the primary galaxy has fewer than five analogs. Some of the analog galaxies selected as a result of similarity to an early primary may in fact be more similar to a primary selected later in the process. Each analog galaxy is therefore compared to all the primaries and reassigned to the group whose primary is most similar (smallest b-value). This finalizes the grouping method for the composite SEDs.

In what follows we work only with groups of at least 19 galaxies (with two exceptions), which allows for good characterization of the intrinsic SED shapes (see Sections 3.4 and 3.5). Groups of galaxies that passed our cuts but were not placed into composite SEDs owing to their small group numbers were inspected as well—these are susceptible to noisy observations. While we require $S/N > 20$ for the K_s detection bandpass, other bands for these galaxies may have lower S/N. If photometry in several bands is particularly noisy in the same direction, a group of galaxies may fail the similarity criteria and be placed into separate groups.
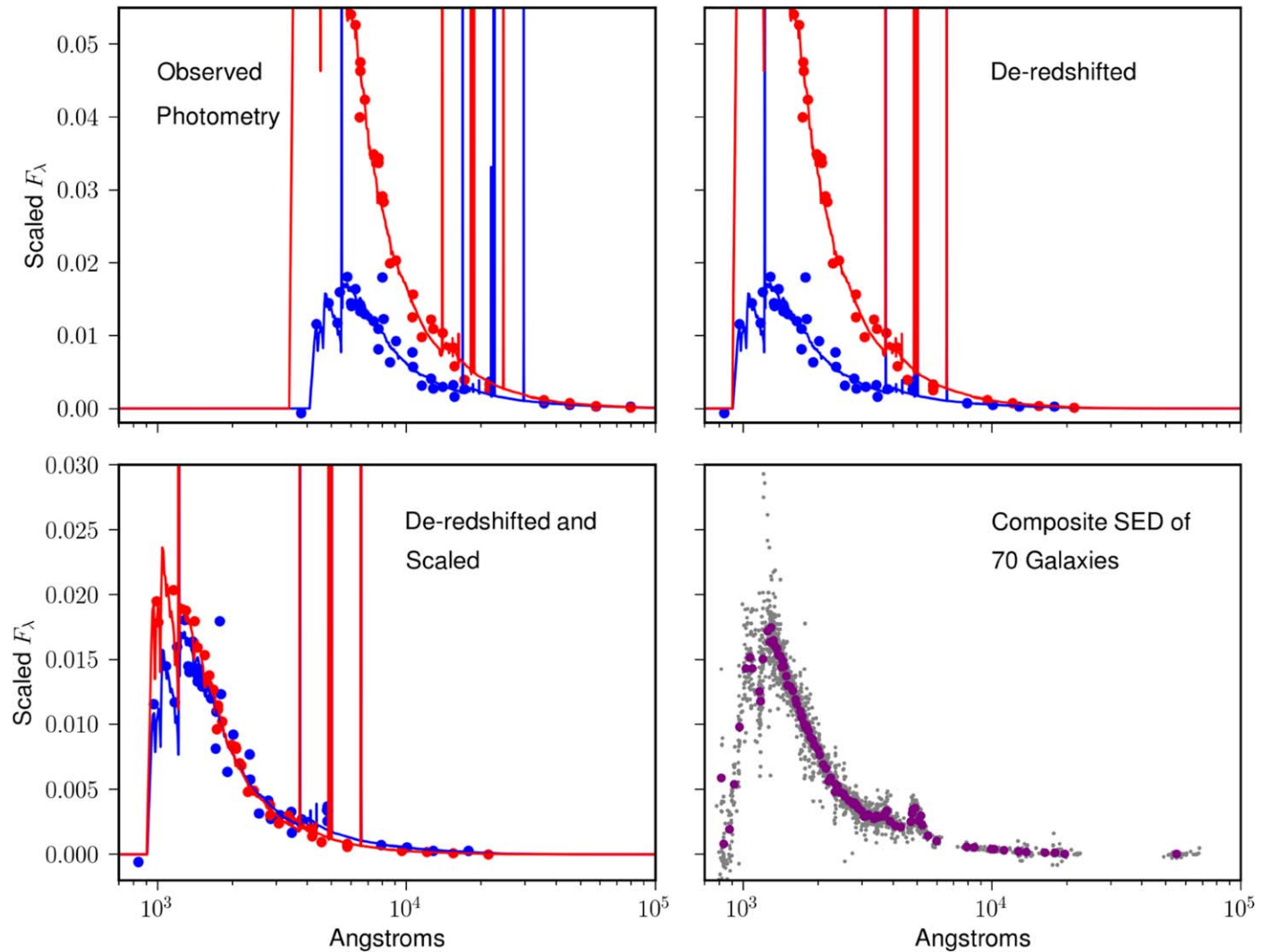
Figure 2. Basic method of composite SED construction. The observed photometry (points) and best-fit SEDs of two similar galaxies are shown in the top left panel. These are deredshifted (top right) and scaled to match (bottom left), effectively doubling the resolution of the photometry. With a significant number of galaxies, a composite SED with impressive spectral resolution ($R \sim 50$ in the near-UV to optical) can be derived from photometric observations alone. An example is shown in the bottom right, with photometric observations in gray and median points in purple.

As a result, many of these small groups look very similar to other composites in, e.g., the optical wavelengths, but offset with noisy observations in, e.g., the near-infrared. While the possibility exists that these are an intrinsically separate population, these galaxies are a larger fraction of the $2.5 < z < 4$ sample consistent with the effects of noise. Regardless, no group appears to have a drastically different SED shape overall, and merging a group with another similar SED shape would not affect our results owing to their small numbers.

The associated observed photometry for each galaxy in a composite SED is deredshifted using ZFOURGE redshifts and scaled using the a value from Equation (2), which in concert probe the underlying SED with greater resolution than is possible with photometry of a single galaxy alone. We split these deredshifted, scaled photometric points into rest-frame wavelength bins with equal numbers of observations. The bins therefore are not necessarily equal in wavelength width, nor are they the same between different composite SEDs. Medians of the deredshifted, scaled photometry in each wavelength bin are taken, generating the composite SED, as shown in Figure 2.

There are nondetections in the data, particularly for quiescent galaxies (QGs) in the UV, and we include these when calculating the composite SED points (i.e., negative fluxes are included when calculating medians). If the median signal for the analog points in a bin has $S/N < 1$, the associated composite SED point is considered an upper limit. This is often seen in the far-UV and near-IR regions of the composite SEDs, where there is little flux relative to instrument sensitivities. The final sets of composite SEDs are shown in the Appendix.

3.3. Custom Composite SED Filter Curves

Median values of the deredshifted, scaled photometric values in each wavelength bin are the composite SED points. Each of these median points also has an associated composite filter response curve, which is a linear combination of the deredshifted photometric filters. A given filter curve is compressed into the observed galaxy rest frame and scaled (using a value k) such that there is equal area (C) under the resulting response curve:

$$\lambda_{\mathrm{comp}} = \lambda_{\mathrm{filter,rest}}/(1 + z) \qquad (3)$$

$$C = k \int_{\lambda_{\mathrm{comp,min}}}^{\lambda_{\mathrm{comp,max}}} R_{\mathrm{filter,rest}} d\lambda_{\mathrm{comp}}. \qquad (4)$$

These deredshifted, scaled filter curves are then summed to obtain the composite SED filter curve. This method ensures that each photometric observation is equally weighted and contributes the same amount to the composite filter response curve. The filter curves allow the characterization of the composite SEDs using EAZY and Fitting and Assessment of Synthetic Templates (FAST; Kriek et al. 2009).

3.4. Composite SEDs at 2.5 < z < 4.0

The ZFOURGE catalogs have 1294 galaxies at $2.5 < z < 4.0$ with the requisite S/N, use flag, and non-AGN identifiers. Of these, 944 (72.9%) are placed into 16 groups based on SED similarity. The resulting composite SEDs are composed entirely of blue galaxies, which are not particularly dusty (90% have $A_V \leqslant 0.9$ mag). An analysis of the sample shows that around 100 of those not initially placed in a group are in fact dusty star-forming galaxies (SFGs) or QGs (based on position in the *UVJ* diagram). However, their SED shapes are different enough to not be grouped together using the above method. For these populations we increase the *b*-parameter cutoff to $b < 0.15$ to recover two *UVJ*-quiescent groups (44 galaxies) and two dusty star-forming groups (49 galaxies), all of which show slightly more scatter than our blue composite SEDs. In total, we therefore have 20 composite SEDs composed of 1037 galaxies (80.1% of the sample that passed our cuts).

The 90% mass completeness of ZFOURGE at $z = 3$ is $\log_{10}(M_{90}/M_{\odot}) \sim 10$ (Tomczak et al. 2016). However, there are a number of galaxies with strong [O III] and Hβ emission in our detection bandpass, K_s. We therefore are sensitive to objects with particularly strong emission from these lines at lower masses than those galaxies without this emission.

The method used to generate these composite SEDs has small methodological changes to that used in Forrest et al. (2017). These changes allow inclusion of a larger number of galaxies in the composite SEDs. The extreme and strong ELGs from Forrest et al. (2017) are now split into several composite SEDs, the differences largely driven by the UV slope of a galaxy.

3.5. Rebuilding Composite SEDs at 1 < z < 3 from Forrest et al. (2016)

For consistency with the new composite SEDs constructed here, we also rebuild composite SEDs at $1.0 < z < 3.0$ using the publicly released ZFOURGE catalogs (v3.4). The composite SEDs presented in Forrest et al. (2016) used an earlier version of the ZFOURGE catalogs. This version did not use the same deep stacked K_s-band detection image and thus was limited to 3984 galaxies in the $1 < z < 3$ sample that also met the other requirements above, namely, having $S/N_{K_s} > 20$ and use = 1. Using the updated catalogs, we obtain 7351 galaxies with the same criteria. The resulting 71 composite SEDs have 6314 galaxies, or 85.9% of the original sample, and unlike the initial grouping at $2.5 < z < 4.0$, they include a number of quiescent and dusty star-forming composite SEDs. One of the groups with fewer than 19 galaxies is also of interest, however, as it contains 14 galaxies with very blue colors and strong emission features, consistent with the ELG seen in the higher-redshift

sample. We thus include this composite SED in our following analysis. ZFOURGE completeness is $\log_{10}(M_{90}/M_{\odot}) \sim 9$ at $z = 1.5$ (Tomczak et al. 2016), and 524 (8.3%) galaxies in our $1 < z < 3$ sample are less massive than this owing in part to Hα falling in the K_s bandpass at $2 < z < 2.5$.

Between the two sets of composite SEDs, there are 6921 total galaxies, i.e., there are 444 galaxies that fall in the redshift range $2.5 < z < 3$ and are in composite groups in both regimes. In this work, we use only these newly constructed composite SEDs and not those previously studied in Forrest et al. (2016, 2017).

4. Measuring Individual Galaxy and Composite SED Properties

In this section we discuss the measurement of quantities that are used in our analysis (Sections 5 and 6). For our analysis of the composite SEDs, we consider both the properties of the analog galaxies and the properties of the composite SED itself. When composite SED "fluxes" are described, these values are scaled as a result of the construction method of the composite SED. As a result, these can only be used validly as part of a color.

4.1. Rest-frame Colors

We consider the *UVJ* diagram in our analysis. Rest-frame fluxes for analog galaxies are taken from the ZFOURGE data release. These values are calculated using EAZY and the nine different galaxy templates mentioned above. We use this same method with our composite SEDs and their custom filter curves to generate rest-frame colors for each composite SED.

4.2. Using Emission-line Templates with FAST

As shown in previous work, failure to account for emission lines when fitting templates to galaxy photometry can lead to severe errors in parameter estimation for the strongest emitters (e.g., Stark et al. 2013; Salmon et al. 2015; Forrest et al. 2017). We therefore refit all of the galaxies in our sample using FAST (Kriek et al. 2011) and a series of models from Bruzual & Charlot (2003, hereafter BC03) with emission lines added.

These emission lines are based on modeling done with CLOUDY 08.00 (Ferland et al. 1998), with methods from Inoue (2011) and Salmon et al. (2015; see Section 3.2). Briefly, the ionization parameter, metallicity, and density of hydrogen are varied to produce sets of emission-line ratios from Lyα to 1 μm. These emission lines are added to the BC03 high-resolution models and are used in our FAST runs. We use a Chabrier (2003) initial mass function, a Kriek & Conroy (2013) dust law, and an exponentially declining star formation history (SFH). All of these assumptions can have effects on our results, in particular dust and age determinations. We do not explore these issues in depth here, but we refer the reader to Cassarà et al. (2016) and Leja et al. (2017) for more information.

We refit all galaxies in our composite SED samples with this set of emission-line models, allowing other parameters to range as in the ZFOURGE catalogs. No galaxies were assigned an age greater than the age of the universe at the corresponding photometric redshift. The differences from these new fits and the ZFOURGE results are non-negligible, showing two main groups (see Figure 3).

The first group consists of galaxies with emission lines, for which models sans emission lines overestimate the mass by
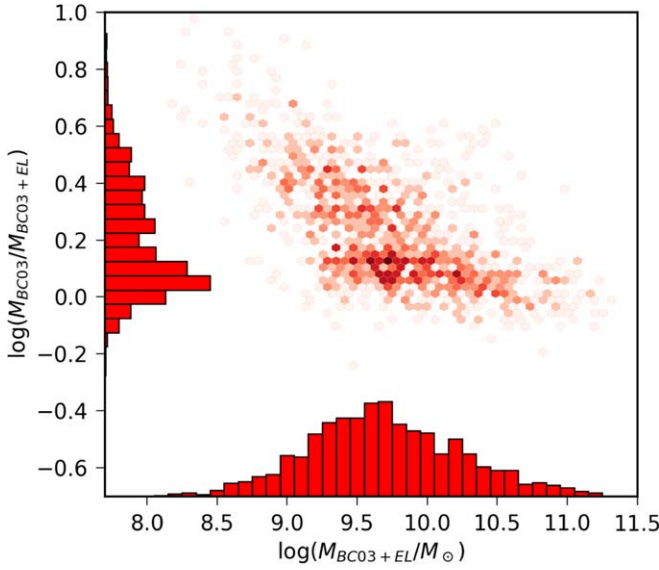
Figure 3. Differences in best-fit mass from FAST for galaxies in our $2.5 < z < 4$ sample. The masses of low-mass galaxies are significantly overestimated if the effects of strong emission lines are not accounted for. These emission lines show effects on galaxies up to $\log(M/M_\odot) \sim 10$.

0.75 ± 0.12 dex at $\log_{10}(M/M_\odot) \sim 8.5$, decreasing to agreement at $\log_{10}(M/M_\odot) \sim 10.5$. The second group does not have strong emission features, and the masses are therefore consistent between the two fits. On average, this second group is higher mass, and the greater stellar continua reduce the effects of any nebular emission lines on SED fitting, although some galaxies down to $\log_{10}(M/M_\odot) \lesssim 9.5$ show little evidence of emission.

The composite SEDs are also fit with FAST. Similar to fluxes, the output masses and SFRs are scaled to unphysical values, although properties such as sSFR, age, and dust attenuation (A_V) are unaffected. For such affected properties, we use the median of the analog population as a characteristic value for the composite SEDs.

4.3. UV Slope

We fit a power law to the composite SED points within the wavelength range $1500 < \lambda/\text{Å} < 2600$, $F \propto \lambda^\beta$ to obtain the UV slope, β. This effectively prevents contamination from Lyα emission, as changing the Lyα template flux yields no change in the fit UV slope. We also masked around the 2175 Å dust feature and refit the power law. For the vast majority of composite SEDs this makes no difference to the fit. In the several cases that show clear attenuation at this wavelength, we mask points over $2000 < \lambda/\text{Å} < 2350$ and use the resultant exponent.

4.4. D(4000)

The 4000 Å break ($D(4000)$) is defined in Bruzual (1983) as

$$D(4000) = \frac{(\lambda^2_{\text{blue}} - \lambda^1_{\text{blue}}) \int_{\lambda^1_{\text{red}}}^{\lambda^2_{\text{red}}} f_\nu \, d\lambda}{(\lambda^2_{\text{red}} - \lambda^1_{\text{red}}) \int_{\lambda^1_{\text{blue}}}^{\lambda^2_{\text{blue}}} f_\nu \, d\lambda}, \tag{5}$$

with $(\lambda^1_{\text{blue}}, \lambda^2_{\text{blue}}, \lambda^1_{\text{red}}, \lambda^2_{\text{red}}) = (3750, 3950, 4050, 4250)$ Å. Given the limited resolution of our composite SEDs, these

integrals generally correspond to two points on either side of the break but are still well constrained.

Several of the ELG composite SEDs have $D(4000) < 1$. This indicates stellar populations dominated by light from young, massive O stars (e.g., Poggianti & Barbaro 1997) and is also influenced by any nebular continuum emission that is present (Byler et al. 2017, 2018). Our composite SED bandwidth also means that our $D(4000)$ calculation is sensitive to the Balmer break and strong emission from [O II] $\lambda 3727$, which for the most extreme emitters could lower our measured $D(4000)$ by up to 0.2. Errors are determined by calculating $D(4000)$ using the 1σ error flux values for the composite SED points. As detailed in Appendix C of Kriek et al. (2011), our photometric redshift errors are sufficiently small that they will not affect this measurement.

4.5. Equivalent Widths

We measure the rest-frame equivalent width (EW) of [O III] $\lambda\lambda 5007, 4959 + \text{H}\beta \, \lambda 4861$ for all of our composite SEDs and Hα+[N II]+[S II] for our $1 < z < 3$ composite SEDs. For the $2.5 < z < 4.0$ sample, the Hα+[N II]+[S II] line blend falls between the K_s band and the IRAC 3.6 μm filter and will therefore not be observable until the *James Webb Space Telescope* (*JWST*) is taking data. To measure the EWs of these line blends, we use the best-fit SEDs from FAST models with emission lines, as described above. We remove the emission lines from these best-fit SEDs to obtain the stellar continuum, and we convolve this with the custom composite SED filters to obtain synthetic photometry of the continuum. The composite SED is then normalized by this synthetic photometry.

Several ways of measuring the EW were tested, two of which are shown in Figure 4. First, we perform a simple trapezoidal integration under the continuum-normalized composite SED in the area of interest,

$$\text{EW}_{\text{[O III]blend}} = \int_{4361}^{5507} (1 - f_\lambda/f_c) d\lambda \tag{6}$$

$$\text{EW}_{\text{H}\alpha\text{blend}} = \int_{5763}^{7363} (1 - f_\lambda/f_c) d\lambda, \tag{7}$$

where f_λ is the composite SED flux and f_c is the continuum flux from the best-fit SED. We note that the composite SED points themselves must be within these limits and therefore are nominally in a narrower wavelength regime. However, since the custom composite SED filters are fairly broad, signals outside of these wavelength limits are in fact being probed. This would be the case even if a single composite SED point were used.

In addition, we fit a Gaussian profile to the continuum-normalized composite SED and integrate under that curve. The results are generally similar to within 10%. However, in some cases, the composite SED points have spacing that yields a discrepancy between the two methods, as can be seen with the Hα emission in Figure 4. In these cases, the fits were visually inspected, and in all such cases the Gaussian profile fit was judged to be superior.

For blends of multiple lines, such as [O III] $\lambda\lambda 5007, 4959 + \text{H}\beta \, \lambda 4861$, we also attempted fitting multiple Gaussian curves, one to each line. Forcing the center of each Gaussian profile to be at the emission wavelength provides a good overall fit to the data, but the individual curves are often unphysical, usually showing strong absorption in one Gaussian profile and strong
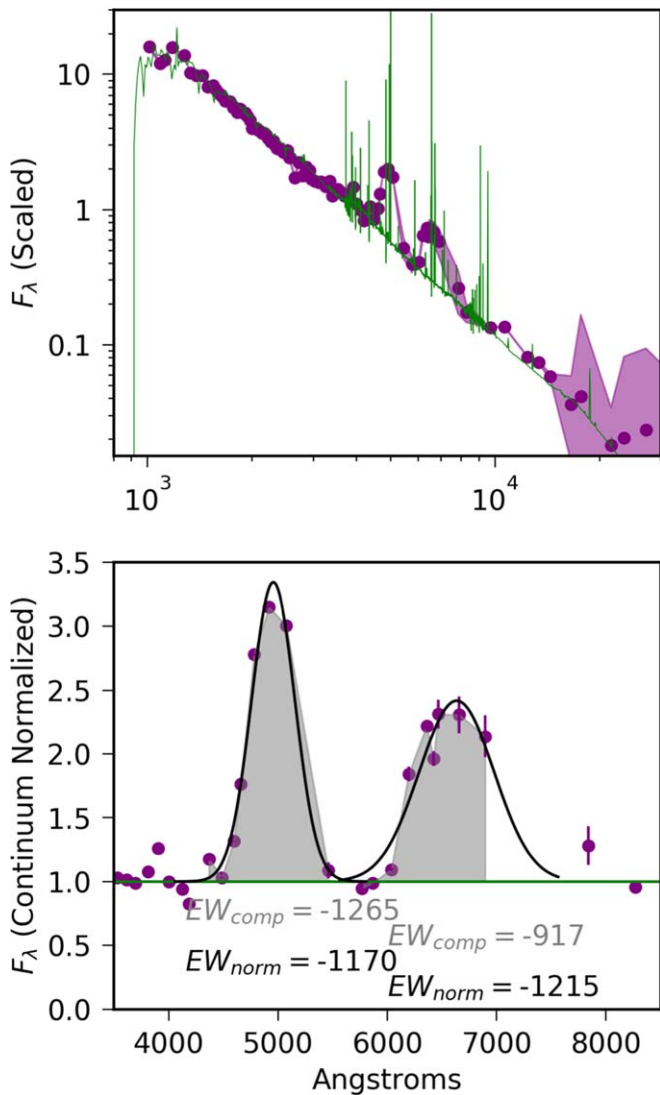
Figure 4. EW determination. Top: bluest composite SED from galaxies at $1 < z < 3$ as determined by UV slope, β. The median composite SED points and associated errors on medians are shown in purple. The best-fit emission-line SED is in green. Bottom: continuum-normalized flux of the composite SED points showing [O III]+Hβ and Hα emission. The black curves show fits of Gaussian profiles to the emission-line blends, while the gray shading shows a simple trapezoidal integration to obtain the EW. In general, these two methods agree within 10%, although in cases of extreme emission such as this, the selection of points for trapezoidal integration is an important factor and can lead to larger discrepancies. Throughout this work, we quote EWs from the Gaussian curve fits.

emission in another. Further constraining this multi-Gaussian profile fit by forcing a line ratio, e.g., [O III] $\lambda5007$/[O III] $\lambda4959 = 3$, generally results in fitting absorption for Hβ, which we take to be unphysical as well given the large Hα EWs. The overall fits are again good, and very similar to the fit of the single Gaussian curve above. EWs measured from the Gaussian profiles are in both cases within a few percent of the single curve fit. The broadness of the custom composite SED filters is the cause of this, as we do not accurately resolve out the different lines.

Weak emission is difficult to quantify accurately, especially when the continuum fit is not good or the composite SED is noisy relative to the line. In general, we are confident in emission EWs down to 20 Å, and most composite SEDs have

[O III]+Hβ and Hα EWs greater than this. In the remainder of this paper, referenced EWs will be from the single Gaussian profile fit for each line blend, and all values will be in the rest frame.

4.6. Morphology

The ZFOURGE data release includes a catalog of sources cross-matched with the CANDELS morphological catalogs of van der Wel et al. (2012). The resolution of the *HST*–F160W imagery used in these catalogs is $0\farcs06$ after drizzling. While at high redshifts this nominally makes fitting small galaxies difficult, van der Wel et al. (2012) find that galaxies with half-light radii of 0.3 pixels are recovered correctly using GALFIT (Peng et al. 2010). There are 31 galaxies in our sample across a range of redshifts and composite SEDs that have fit sizes below this limit—excluding these galaxies makes no difference in our results. We compare sizes and Sérsic indices for galaxies of different classifications in Section 6.3.

5. Spectral Feature Analysis

5.1. Composite SED Classification

In this work we classify our composite SEDs that show evidence of star formation by their $D(4000)$, Hα, and [O III] emission line strengths and dust attenuation (see Figure 5). $D(4000)$ is a proxy for age (e.g., Poggianti & Barbaro 1997), although with a dependence on metallicity (e.g., Kauffmann et al. 2003). Hα probes the star formation activity for galaxies in a composite SED (e.g., Kennicutt & Evans 2012). While [O III] emission is dependent on abundances, it is also sensitive to ionizing photons from young stars.

It should be noted that both emission features as measured from the composite SEDs are blends. Hα is blended with [N II] and [S II] lines but will dominate the signal for strongly SFGs; while [O III] is blended with Hβ, the oxygen will similarly dominate for the strongest emitters (e.g., Baldwin et al. 1981; Kewley et al. 2013). Using these parameters derived from the composite SEDs means that this selection is independent of the morphologies of the galaxies involved and is less sensitive to photometric errors than color selections for individual galaxies. Nonetheless, as described below, we still pick out trends in both parameters based on our classification.

The majority of our composite SEDs have $EW_{H\alpha} \sim 100$ Å, and these are classified as SFGs. With increasing $D(4000)$ we see this EW decrease, as well as an increase in dust attenuation as fit by FAST, in agreement with Figure 8 from Kriek et al. (2011). However, there are several composite SEDs with $D(4000) \gtrsim 1.5$ and $30 \lesssim EW_{H\alpha}/Å \lesssim 50$ that show less dust than other composite SEDs at similar values. These are classified as TGs, which will be discussed in greater detail in Section 7.

At low $D(4000)$ we see groups with large $EW_{H\alpha}$ (and $EW_{[O III]+H\beta} > 400$ Å), which we classify as extreme ELGs. A slightly different set of composite SEDs with many of the same galaxies is discussed in more detail in Forrest et al. (2017).

While the SFGs have $D(4000) \sim 1.3 \pm 0.2$ and $\log_{10}(EW_{H\alpha}/Å) \sim 2^{+0.2}_{-0.1}$, several composite SEDs have $D(4000) > 1.5$ and $EW_{H\alpha} < 20$ Å. Upon visual inspection, we classify these as either QGs or PSBs based on the sharpness and location of the turnover of the SED around 5000 Å. While dusty SFGs, TGs, and QGs all have a plateau in the SED from 0.5 to 0.7 μm (in F_λ units), the PSBs have a distinct peak blueward of this, consistent
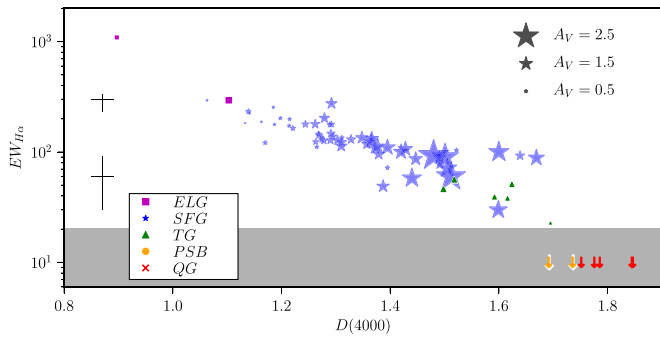
Figure 5. Hα EW$_{REST}$ against $D(4000)$ for our $1 < z < 3$ composite SEDs. This is used in concert with the [O III]+Hβ EW$_{REST}$ and dust attenuation fit using FAST, indicated by marker size, to classify the composite SEDs that show evidence of star formation. SFG composite SEDs (blue stars) show a trend toward larger dust attenuation and lower Hα EW$_{REST}$ at higher $D(4000)$. TGs (green triangles) show significantly less dust for their $D(4000)$, bucking the trend of the other SFGs. Those classified as extreme ELGs are shown as magenta squares, which have $D(4000) < 1.1$ as well as EW$_{[O\ III]} > 400$ Å. PSGs (orange) and QGs (red) are not detected above our noise threshold of 20 Å (gray shaded region). Representative error bars are shown on the left. We emphasize that these are errors on the composite SED measurements and do not convey the scatter in the underlying galaxy populations.

with the populations of A-type stars that helped lead to their original moniker—E+A galaxies. Figure 6 shows the optical wavelengths for examples of the different classes.

The composite SEDs constructed from galaxies at $2.5 < z < 4$ lack coverage across wavelengths to which Hα is redshifted—the line falls between the K_s band and the IRAC channels. We again use $D(4000)$ and EW$_{[O\ III]+Hβ}$ to identify three ELG composite SEDs, and we use visual identification to compare the others to the low-redshift sample. There is less variety seen than at $1 < z < 3$, with 15 of the 19 composite SEDs clearly falling into the star-forming regime, including the two dusty composite SEDs. The remaining two, constructed from UVJ–QGs, show some scatter but appear most similar to the PSBs from the $1 < z < 3$ sample. While there may be a few older QGs in these samples, they are in the minority.

In what follows, we compare the properties of galaxies in these different classes. On the whole, reassigning a single composite SED to a different class (within reason, i.e., SFG to/from TG or PSB to/from QG) does not affect our conclusions. Throughout the paper, we will use purple to represent ELGs, blue for SFGs, green for TGs, orange for PSBs, and red for QGs.

5.2. EW–Mass

The use of deep narrowband imaging to find ELGs in specific redshift windows has been used for over 2 decades (e.g., Hu & McMahon 1996; Cowie & Hu 1998; Teplitz et al. 1999), notably in the High Redshift Emission Line Survey (HiZELS; Geach et al. 2008). More recently, ELGs have also been identified from flux excesses in broadband filters relative to adjacent multiwavelength photometry (e.g., Fumagalli et al. 2012; Finkelstein et al. 2013; Labbé et al. 2013; Stark et al. 2013; Smit et al. 2014). Composite SEDs have been used for ELG selection as well (Kriek et al. 2011; Forrest et al. 2017).

Using these large numbers of EWs, trends have been found with mass and redshift. Fumagalli et al. (2012) use data from
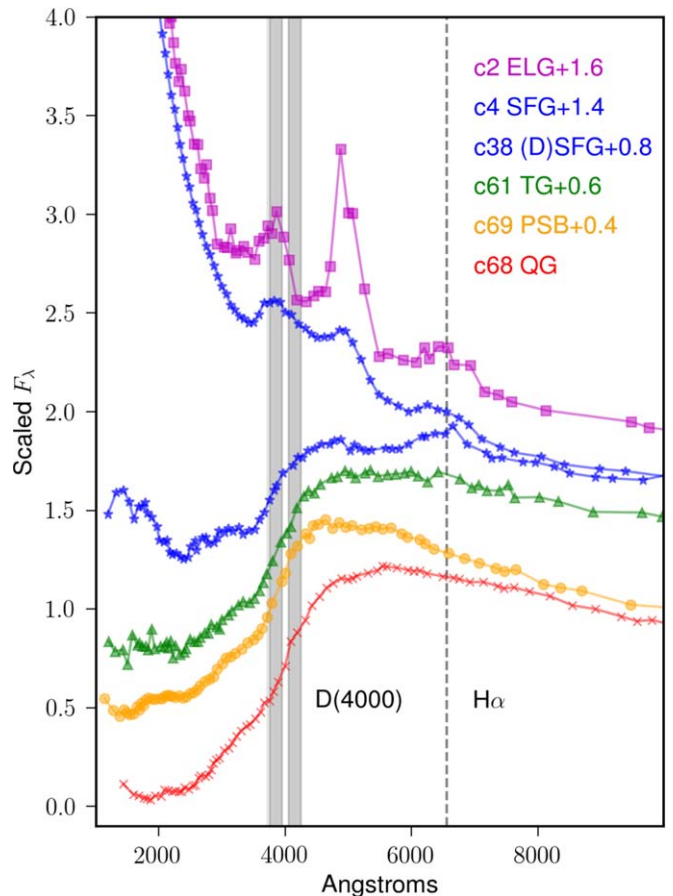
Figure 6. Several representative composite SEDs showing the rest-frame optical wavelengths. These are plotted with a vertical offset for clarity. The composite ID for reference with the Appendix is given. We are able to discern between the quiescent and post-starburst composite SEDs owing to the sharper turnover of the PSBs. That is, the spectral peak redward of the 4000 Å break is blueward of ~4500 Å for PSBs, while older quiescent populations peak redward of 5000 Å. Blue SFGs and extreme ELGs have considerably more UV–optical flux than any of the other types shown here. IDs given are for reference with data in the Appendix—all composite SEDs shown here are from the $1 < z < 3$ set.

3D-*HST* to quantify Hα+[N II] EW against mass across several redshifts and find that, for galaxies of a given mass, EWs are higher at higher redshift, similar to results from HiZELS (Sobral et al. 2013). Similarly, data from HiZELS (Khostovan et al. 2016) and *Spitzer* (Smit et al. 2015) have been used to trace out [O III]+Hβ EWs against mass, with similar conclusions. Specifically, [O III]+Hβ EWs for galaxies of a given mass appear to have decreased since $z \sim 2.5$.

The Hα EWs for the $1 < z < 3$ sample are in good agreement with both Fumagalli et al. (2012) and Sobral et al. (2013) (see top right panel of Figure 7). Unfortunately, we are unable to probe Hα+[N II] in our $2.5 < z < 4$ sample to see whether this ratio varies with redshift, but this will be explored by *JWST*.

Interestingly, our results for [O III]+Hβ diverge from HiZELS work (Khostovan et al. 2016). In the $1 < z < 3$ sample we have good agreement at $\log(M/M_\odot) \sim 9$ but more extreme emitters and fewer massive emitters. The picture is similar in $2.5 < z < 4$, except that the samples agree at $\log(M/M_\odot) \sim 9.5$.
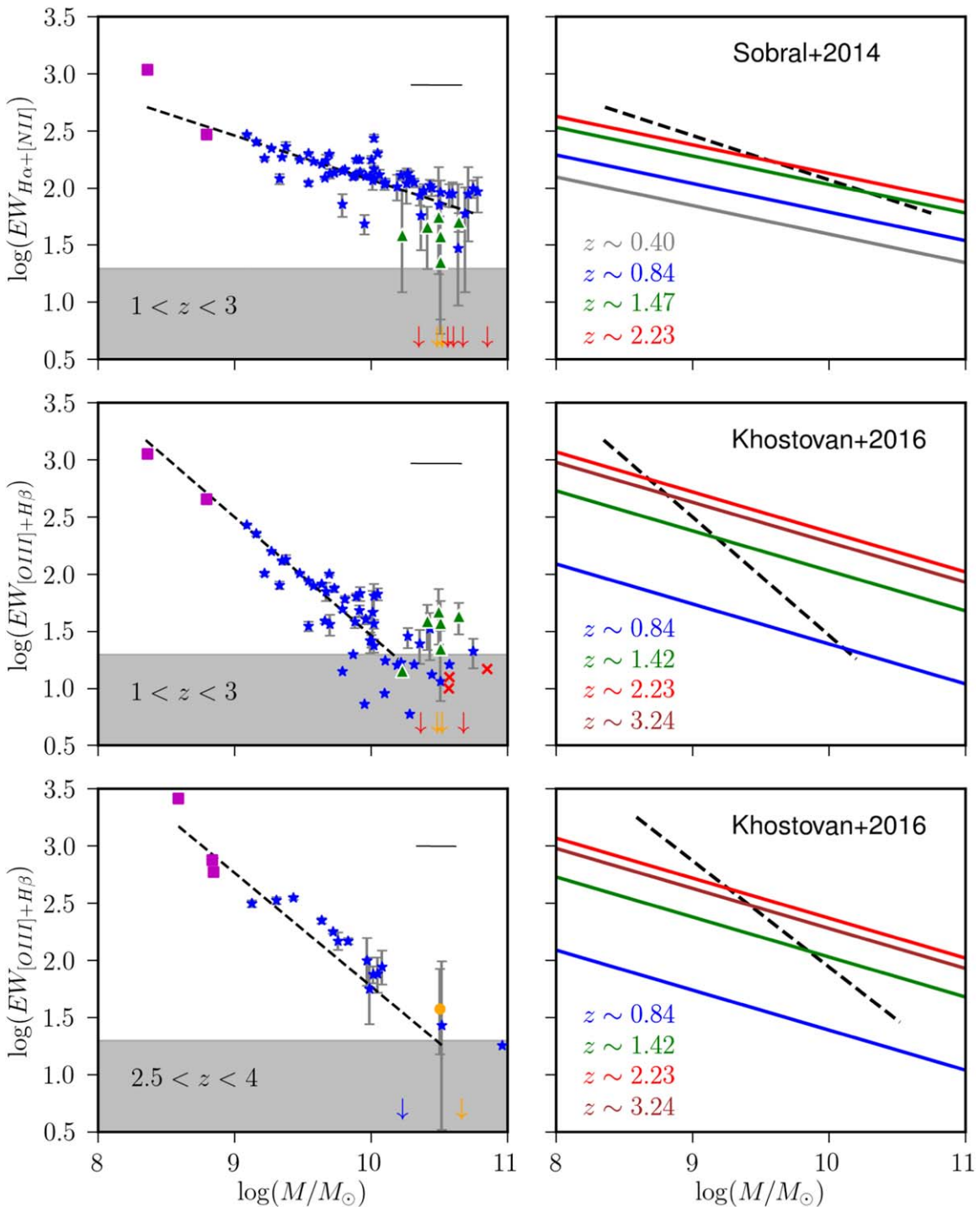
Figure 7. EWs against mass for the composite SEDs, with points colored according to the classification as in previous figures (see Figure 5). The gray shaded regions represent EW < 20 Å, which we take to be the limit of our sensitivity with the composite SEDs. Masses are medians of the analogs in a composite SED. Typical standard deviations for the masses in a composite SED are 0.3 dex for $1 < z < 3$ and 0.25 dex for $2.5 < z < 4$, shown by the black error bar in the upper right corner of the left panels. Top left: Hα+[N II] EW for composite SEDs at $1 < z < 3$. Middle left: [O III]+Hβ EW for composite SEDs at $1 < z < 3$. Bottom left: [O III]+Hβ EW for composite SEDs at $2.5 < z < 4$. Right: fits to composite SED EWs shown as black lines, with relations from Khostovan et al. (2016; middle, bottom) and Sobral et al. (2013; top) shown as colored lines.

We note that our sample is not mass complete down to the lowest masses, as only low-mass galaxies with strong emission lines in the K_s band will be included. As seen in Table 1, the composite SEDs do not have any galaxies of similar mass to the ELGs (below $\log(M/M_\odot) \sim 9$) without such remarkable emission. As a result, our large-EW (low-mass) end of the sample is skewed upward. Also, the composite SEDs are not

sensitive to weak emission that can be found in more massive SFGs. Khostovan et al. (2016) note these factors in the HiZELS sample as well, but they find that these biases do not affect the EW−mass relation significantly.

The remaining difference between our samples is the width of our redshift bins, across which lines move in and out of the K_s band (our detection bandpass). At $2 < z < 2.5$, Hα

Table 1
Average Parameters of Different Classes

	Class	$N_{\rm comp}$	$\log_{10}(M/M_\odot)$	$EW_{\rm [O\,III]}$ (Å)	$EW_{\rm H\alpha}$ (Å)	$D(4000)$	A_V	r_e	n
$1.0 < z < 3.0$	ELG	2	$8.66^{+0.47}_{-0.40}$	794^{+230}_{-230}	693^{+271}_{-271}	$1.00^{+0.07}_{-0.07}$	$0.45^{+0.38}_{-0.29}$	$1.1^{+1.2}_{-0.5}$	$1.8^{+1.3}_{-1.2}$
	SFG	57	$9.59^{+0.55}_{-0.42}$	34^{+48}_{-30}	127^{+56}_{-37}	$1.30^{+0.18}_{-0.10}$	$0.60^{+0.60}_{-0.40}$	$2.4^{+1.8}_{-1.1}$	$1.2^{+1.1}_{-0.6}$
	SFG_{MM}	18	$10.48^{+0.36}_{-0.42}$	-4^{+18}_{-19}	93^{+17}_{-63}	$1.46^{+0.14}_{-0.08}$	$1.70^{+0.70}_{-0.60}$	$3.4^{+2.0}_{-1.4}$	$1.2^{+1.1}_{-0.6}$
	TG	6	$10.52^{+0.34}_{-0.51}$	38^{+6}_{-17}	42^{+10}_{-7}	$1.60^{+0.04}_{-0.08}$	$0.70^{+0.70}_{-0.50}$	$2.0^{+2.1}_{-1.0}$	$2.9^{+2.0}_{-1.4}$
	PSB	2	$10.51^{+0.35}_{-0.38}$	-16^{+12}_{-12}	-13^{+9}_{-9}	$1.71^{+0.02}_{-0.02}$	$0.40^{+0.20}_{-0.30}$	$1.0^{+1.0}_{-0.4}$	$3.4^{+1.7}_{-1.0}$
	QG	5	$10.61^{+0.33}_{-0.39}$	10^{+3}_{-14}	2^{+2}_{-4}	$1.78^{+0.06}_{-0.02}$	$0.40^{+0.40}_{-0.20}$	$1.5^{+1.4}_{-0.6}$	$3.5^{+1.8}_{-1.2}$
$2.5 < z < 4.0$	ELG	3	$8.82^{+0.72}_{-0.31}$	755^{+1276}_{-106}	$\cdots$	$0.94^{+0.03}_{-0.02}$	$0.60^{+0.20}_{-0.50}$	$1.2^{+1.1}_{-0.7}$	$1.2^{+1.5}_{-0.9}$
	SFG	15	$9.77^{+0.39}_{-0.32}$	100^{+193}_{-66}	$\cdots$	$1.23^{+0.06}_{-0.06}$	$0.40^{+0.50}_{-0.30}$	$1.8^{+1.3}_{-0.8}$	$1.2^{+1.4}_{-0.6}$
	PSB	2	$10.63^{+0.32}_{-0.34}$	8^{+20}_{-20}	$\cdots$	$1.66^{+0.03}_{-0.04}$	$0.50^{+0.31}_{-0.20}$	$1.0^{+0.9}_{-0.5}$	$2.8^{+1.8}_{-1.3}$

Note. EWs in emission are listed as positive numbers and, along with $D(4000)$, are measured from the composite SEDs. Other parameters are medians of analog galaxy values, with errors shown the 16th and 84th percentiles.

falls into the K_s band, and [O III]+Hβ does the same at $3 < z < 3.8$.

Regardless, the TGs clearly show reduced Hα emission relative to SFGs of the same mass. Combined with their elevated [O III]+Hβ, this suggests the possibility of AGNs. While the strongest AGN should be removed with the catalogs from Cowley et al. (2016), the possibility of low-level AGN contamination does remain. Rest-frame optical spectroscopic follow-up will allow quantification of such contamination.

6. Photometric Analysis

6.1. Color Relations

The composite SEDs are formed based on multicolor comparisons. As such, we would expect the groups to separate into distinct groups on color–color diagrams, the best known of which is the *UVJ* diagram (e.g., Wuyts et al. 2007; Williams et al. 2009; Whitaker et al. 2012b; Forrest et al. 2016; Straatman et al. 2016). There is a spread in the colors of analogs in a given composite SED, and we display these by calculating 1σ error ellipses based on the covariance between the colors, shown in Figure 8. As expected, composite SEDs in a given class are mostly separated from other classes, although some of the individual galaxy colors do overlap. This indicates that while the *UVJ* diagram does a good job on average discerning between a simple red and blue sequence, it does not yield the whole picture that can be obtained by analyzing the full SED of a galaxy. In this picture, the colors of TGs are consistent with galaxies in the green valley and with the TGs of Pandya et al. (2017).

We note that there is reduced diversity in the $2.5 < z < 4$ composite SEDs. While some of this is due to the reduced sensitivity to objects with faint stellar continua, this does not explain the lack of quiescent objects, nor the lack of transition objects, as ZFOURGE is mass complete for these samples out to $z \sim 3.5$. This is suggestive that these populations are rarer at high redshifts, which is known to be the case for quiescent and dusty objects (e.g., Spitler et al. 2014; Straatman et al. 2016; Glazebrook et al. 2017). Nonetheless, PSBs are found here, implying that star formation has been turned off, or at least significantly reduced, as studies have shown that galaxies in this regime of the *UVJ* diagram can still be forming stars, albeit with low sSFR (e.g., Ciesla et al. 2017).

Additionally, the star-forming sequence of the *UVJ* diagram broadens, suggesting a wider range of colors for SFGs at high redshift. While measurement errors may play a small role here, the intrinsic spread is expected to increase owing to the presumed bursty nature of star formation in young galaxies (e.g., Papovich et al. 2001; Castellano et al. 2014; Izotov et al. 2016), although uncertainties remain on this front (see, e.g., Smit et al. 2015). There are also a greater number of galaxies with strong nebular emission falling in the rest-frame *V* band, which boosts galaxies to particularly blue colors in *(V–J)*.

This classification scheme is also consistent with that determined using a color–mass diagram. We correct the rest-frame *(U–V)* colors using the dust attenuation for a galaxy as described in Brammer et al. (2009) and shown in Figure 9. This correction for dust attenuation more closely approximates the intrinsic colors, providing a clearer separation between dusty SFG, TG, PSB, and QG composite SEDs.

6.2. Star-forming Main Sequence

Previous works have also classified galaxies in narrow redshift bins based solely on sSFR (e.g., Pandya et al. 2017). Figure 10 shows the locations of individual galaxies of different composite SED class on the sSFR–$M_\odot$ plane. While on the whole different classes do separate out nicely, there exists some overlap between TGs and PSBs in the $1 < z < 3$ redshift set. The sSFRs are lower for the PSBs on average, which is reasonable since they are thought to be almost completely quenched, while TGs are in the process of quenching. However, numerous studies have shown an evolution of SFR (and sSFR) against mass as a function of redshift—in general, higher redshifts show fewer quenched galaxies, higher-mass galaxies quenching, and higher SFRs for SFGs of a given mass (e.g., Whitaker et al. 2012b; Behroozi et al. 2013; Sparre et al. 2015; Tomczak et al. 2016; Pandya et al. 2017). Due to the large width of the redshift bins for our composite SEDs, the evolution of these relations is a driver of the scatter observed in Figure 10. Therefore, while we find larger numbers of galaxies with high sSFRs and fewer quenched galaxies at higher redshifts, we do not make any conclusions about the efficacy of galaxy categorization by sSFR.

6.3. Morphological Evolution

We also investigate the morphologies of galaxies with regard to mass and classification, shown in Figure 11. The SFGs match well with previous analyses of the size–mass relation
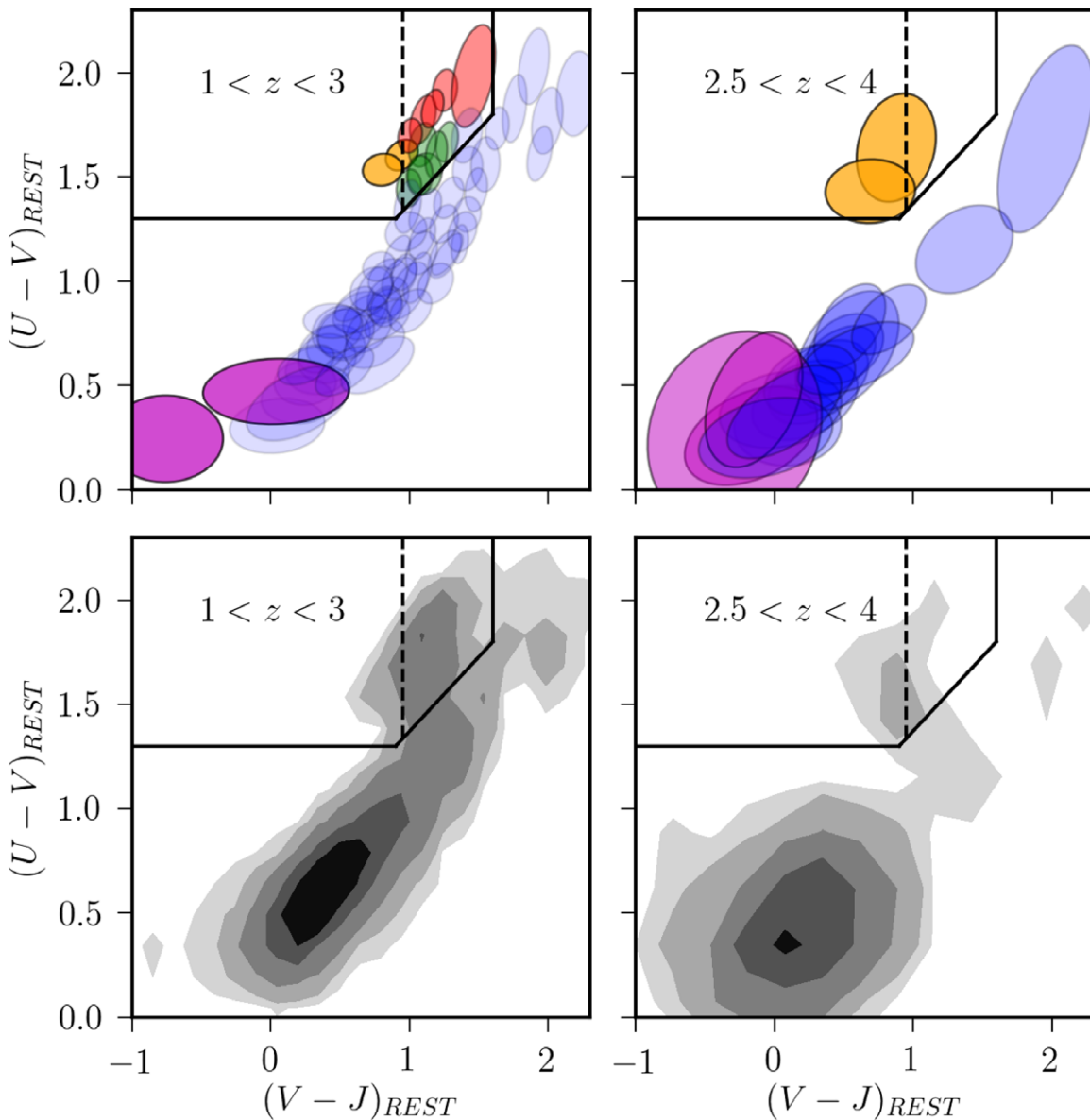
Figure 8. *UVJ* diagram. Top: 1σ error ellipses of our composite SEDs based on analog positions on the *UVJ* diagram. The $1 < z < 3$ composite SEDs are on the left, while $2.5 < z < 4$ composite SEDs are on the right. Star-forming composite SEDs are shown in blue, ELGs in magenta, PSBs in orange, quiescent composite SEDs in red, and transitional composite SEDs in green. The vertical dashed line is from Whitaker et al. (2012a) and Wild et al. (2014) and separates PSBs (blueward) from older QGs (redward). Bottom: contours of analog galaxies on the *UVJ* diagram. Contours for the $1 < z < 3$ sample are 3, 10, 30, 100, and 300 galaxies, while $2.5 < z < 4$ contours are 3, 8, 22, 60, and 120 galaxies.

(e.g., ZFOURGE and COSMOS/UltraVISTA; Allen et al. 2017; Faisst et al. 2017). Additionally, most of the TGs, PSBs, and QGs lie near the selection criterion for compact QGs from Barro et al. (2013).

At $1 < z < 3$, the SFGs have larger sizes than all other galaxy classifications for a given mass. The TGs, in particular, have median sizes half those of the SFGs and twice those of the QGs, as would be expected for galaxies whose star formation is being quenched. Meanwhile, the sizes for PSBs are on average smaller than QGs of the same mass ($\log(p) \sim -7$ from a Kolmogorov–Smirnov [K-S] test).

ELGs and SFGs have similar Sérsic indices of $n \sim 1$, and the PSBs and QGs have values of $n \sim 3.5$ (the distributions are quite similar, with $p = 0.68$ from a K-S test, in agreement with

results from Almaini et al. 2017). Meanwhile, the TGs have values of $n \sim 2$–3. Combined with the Hα EWs, this indicates that morphological changes such as the development of a central bulge are already underway before star formation has ceased completely, although further size growth may occur (see also Papovich et al. 2015).

Additionally, we fit lines to the Sérsic indices of the analog galaxies in a given class against both mass and redshift. No class shows evidence for significant evolution with redshift, with slopes $|\Delta n/\Delta z| < 0.2$, smaller than the spread and errors on the values. All classes except the ELGs show median increases with mass, although such increases are $\Delta n < 1$ over $8.5 < \log(M/M_\odot) < 11.5$, no larger than the distribution of galaxy values for a given mass.
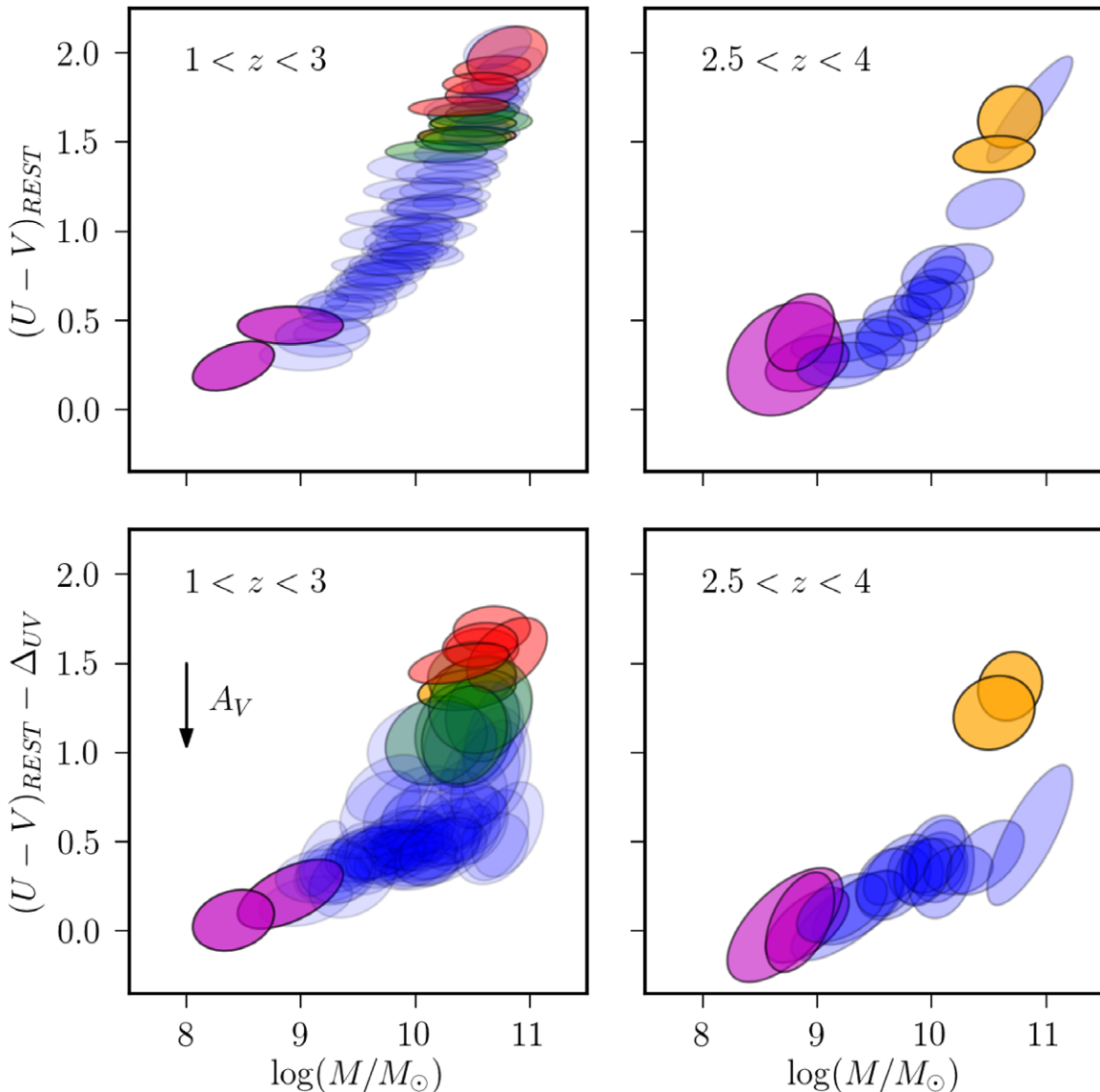
Figure 9. Composite SEDs plotted as 1σ error ellipses of the analogs that compose the composite SED in $(U-V)$–mass. The top rows are colors fit using EAZY, while the bottom row is corrected by dust attenuation derived using FAST. The left column is for galaxies in our sample in $1 < z < 3$, while the right column is for galaxies in $2.5 < z < 4$. The dust correction removes many of the SFGs in the observed green valley.

6.4. Post-starburst and TG Number Densities

We calculate the number densities of TGs, PSBs, and QGs of galaxies in our composite SEDs across redshift space. Additionally, we show number densities for a mass-matched population of massive SFGs, achieved by selecting composite SEDs above a median mass of $\log(M/M_\odot) > 10.25$ and including all galaxies in those composite SEDs. The mass limit was chosen by maximizing the p-value from a two-sample K-S test between the masses of the TGs and selected SFGs ($p = 0.69$). Incidentally, this also yields $p = 0.62$ for masses of the PSBs and selected SFGs. Since a galaxy's stellar mass should not change significantly during the quenching process (ignoring mergers), these mass-matched SFGs should be most similar to progenitors of the TGs and PSBs.

Our results for the PSBs and QGs, shown in Figure 12, are consistent with those from NMBS (Whitaker et al. 2012a) and the UKIDSS Deep Survey (UDS; Wild et al. 2016) at $z \sim 1$–2 and extend out to higher redshifts. The $z \sim 1$ side also lines up

with results from the Galaxy and Mass Assembly and VIMOS Public Extragalactic Redshift Surveys (Rowlands et al. 2018). We note that each of these works selects PSBs in a different manner—Whitaker et al. (2012a) use an age-motivated cut on the *UVJ* diagram, and Wild et al. (2016) use a selection based on PCA colors, while we use composite SEDs to select on population $D(4000)$ and emission-line characteristics.

Comparing the number densities of different groups across a range of redshifts suggests that the transitional phase is even rarer than the traditional post-starburst phase at high redshifts, but it becomes more common at $z < 2$. Additionally, the density of PSBs is relatively constant from $1.5 < z < 3$, with evidence for a turnover at $z \lesssim 1.5$, below which such galaxies become rarer. While the PSB curve stays mostly flat, the shape of the TG curve is more similar to that of the QGs, which increases dramatically from $z = 3$ before beginning to flatten at $z \sim 1.5$. This suggests that the TG population represents a quenching mechanism with a longer timescale than PSBs,
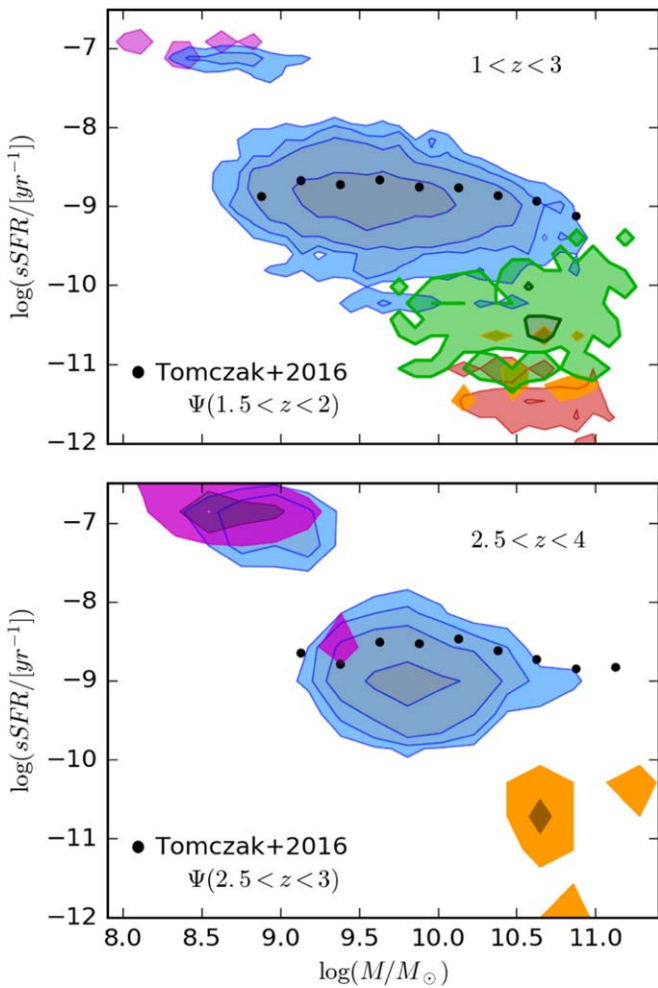
Figure 10. The sSFR–stellar mass relation for galaxies in different composite SED classes. The contours show all galaxies in composite SEDs of a specific classification, using the same color scheme as previous figures. The various classes show separation with respect to sSFR. The black points are the SFR–M_* relations for SFGs from Tomczak et al. (2016) at similar redshifts. While there is some overlap between the TGs and PSBs, the mean sSFR for PSBs is lower. The average sSFR increases at higher redshifts.

which has become more prevalent at later times, discussed in more detail in the following section.

Across $3 < z < 4$ Tomczak et al. (2016) report a ZFOURGE mass completeness limit of $\log_{10}(M/M_\odot) = 10.25$, in agreement with our mass-matching selection. The TGs, PSBs, and QGs have mass distributions with medians $\log_{10}(M/M_\odot) =$ 10.51, 10.54, and 10.61, respectively, in close agreement with the mass-matched SFG population, with a median of $\log_{10}(M/M_\odot) = 10.48$. Due to the similar masses and detection-band magnitudes for members of the TGs, PSBs, and QGs, any biases and selection effects would affect them in a similar manner. While some individual galaxies in our $2.5 < z < 4$ PSB composite SEDs could be quiescent or transitioning, the clear differences in composite SED shape guarantee that they would be few in number. The average properties of these different classes, including the mass-matched SFG sample, are shown in Table 1.

7. Discussion

Our TG classification appears successful in picking out galaxies transitioning between more typical SFGs and QGs.

These galaxies have masses $\log_{10}(M/M_\odot) \sim 10.5$, which are similar to dusty SFGs, PSBs, and QGs. However, there is no evidence of large amounts of dust in the TGs ($A_V \sim 0.7$ mag) compared to dusty SFGs with similar masses ($A_V \sim 1.7$ mag), and they show less Hα emission—EW$_{\rm REST} \sim 40$ Å (vs. $\sim$100 Å for dusty SFGs; Figure 7, Table 1). The red colors and low emission-line EWs are therefore due to fewer O- and B-type stars and low-level residual star formation rather than to heavy dust obscuration, as expected for SFGs of similar mass.

The TGs still show more dust than PSBs and QGs ($A_V \sim 0.4$ mag) and are morphologically different ($r_e/$kpc $\sim$ 2 vs. 1 for PSBs and $n = 2.9$ vs. 3.5; Figure 11, Table 1). K-S, Anderson–Darling, and Mann–Whitney tests for the distributions of TGs and PSBs in dust, size, and Sérsic index reject the hypothesis that the two groups are drawn from the same distribution (p-values of 0.018, 0.014, and 0.025 in the three tests for the Sérsic index, and $\log(p) < -4$ for the A_V and size comparisons in all three tests).

The intermediate changes in morphology that occur in a galaxy while its star formation is being shut off are unclear. Galaxies will generally be disky at early times when they are actively forming stars, and they develop a spheroidal bulge that dominates the morphology at late times after star formation has ceased. A number of recent works have proposed the idea of compaction (Barro et al. 2013; Dekel & Burkert 2014) and morphological quenching (Martig et al. 2009), in which the process of developing this central bulge is in fact the cause of (or due to the same cause as) star formation cessation. Unless morphological changes occur on timescales less than $\sim$10 Myr (the sensitivity of Hα to star formation), we argue that such changes begin before star formation has been completely switched off.

Cessation of star formation in a disk with continued star formation in a central bulge could explain the morphological and EW trends seen. Such a process would lead to the galaxy's light being concentrated in the center, yielding measurements of smaller sizes and larger Sérsic indices while also showing Hα emission. The opposite process, where star formation continues in the disk but shuts off in the bulge, would not show these same effects, contradicting the observations. We do not argue against this happening for individual galaxies, but it appears to not be the case for the majority.

Galaxies in the green valley with similar low-level sSFRs have had several potential explanations proposed. The most common is that these galaxies are in the process of quenching by some as-yet-undetermined mechanism(s), which are likely dependent on both galaxy mass and environment (see Introductions of, e.g., Darvish et al. 2016; Kawinwanichakij et al. 2017; Papovich et al. 2018, for nice summaries). A variety of quenching mechanisms are associated with different timescales for the cessation of star formation. Barro et al. (2013) and Schawinski et al. (2014) showed that galaxies in the green valley of the color–mass diagram are representative of multiple quenching mechanisms and not a single separate population. On the other hand, simulations have claimed that a single timescale of $\lesssim$2 Gyr to cross the green valley is able to match observations (e.g., Trayford et al. 2016; Davé et al. 2017; Nelson et al. 2018; Pandya et al. 2017).

However, there is also the possibility that QGs have had their star formation "rejuvenated" and are thus moving into the green valley from the red side as suggested in both observations (e.g., Rampazzo et al. 2007; Fang et al. 2012; Darvish et al. 2016;
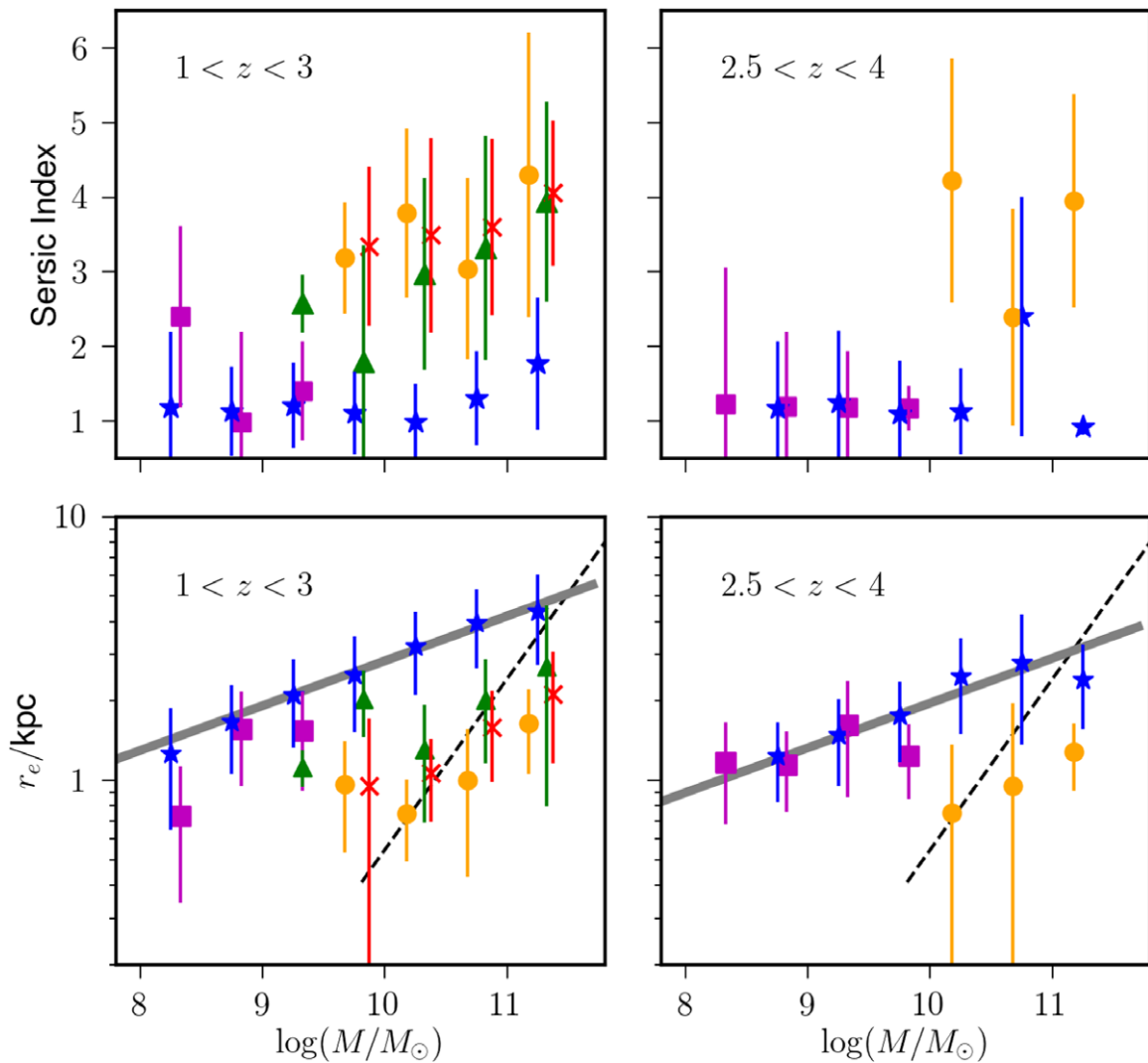
Figure 11. Morphological characteristics of galaxies in different composite SED classes. Top: Sérsic indices for galaxies in our sample according to mass and classification, color-coded as in previous figures. Points are slightly offset along the abscissa for clarity, and error bars show the 16%–84% range in values for analog galaxies in composite SEDs of the class and binned mass range. Bottom: size–mass plane for galaxies in our composite SEDs. The SF galaxies follow the size–mass relations from Allen et al. (2017) (thick gray line) quite well, while at low redshift all other classes are smaller in size for a given mass (left). At $2.5 < z < 4$ (right), the ELGs have similar sizes, while PSBs are smaller. In both cases, the non-star-forming classes lie near the compactness selection criterion of Barro et al. (2013), shown as a dashed line.

Pandya et al. 2017) and simulations (e.g., Davé et al. 2017; Nelson et al. 2018). Such rejuvenation is thought to be rare, and it also results in only a small change in color, which cannot move a previously quenched galaxy to match the colors of galaxies in the blue cloud (Davé et al. 2017; Nelson et al. 2018). While the PSBs have nearly constant number densities across $1.5 < z < 3$ before becoming rarer at lower redshifts, the number density of the TGs in Figure 12 closely follows that of the QGs over the same time, suggesting an evolutionary pathway. The similar numbers also lead us to conclude that rejuvenated galaxies are not a significant fraction of our TGs, though we cannot rule them out entirely.

Another possibility is that SFGs oscillate about the star-forming main sequence, with periods of enhanced and reduced star formation on the order of 0.3 dex (e.g., Tacchella et al. 2016). Not only do simulations suggest that this is more common for lower-mass galaxies (Zolotov et al. 2015), but our TGs also extend over 1 dex below the main sequence, implying that this explanation can only contribute a small portion of the TGs observed.

Recently, Dressler et al. (2018) have noticed a population of "late bloomers," massive galaxies at $z \sim 0.5$ that have formed most of their stellar mass in 2 Gyr before that epoch. These galaxies have some broad similarities to the TGs, including *UVJ* position, stellar mass, and declining SFRs. However, they also have a wider range of SED shapes and morphological properties, preventing us from concluding that they are the similar objects. It should be noted that beyond $z \sim 2.5$ it becomes difficult to *not* have the majority of stellar mass formed in the 2 Gyr before observation owing to the age of the universe at these times. Galaxies with such SFHs would therefore be considerably more common.

A further hypothesis is that all galaxies in the process of quenching will have a post-starburst phase, which is shorter than the overall time in the green valley and either precedes or follows it. The relative number densities of TGs and PSBs conflict with this idea, as the number densities of PSBs are more constant over $1.5 < z < 3.0$, while TGs continue to increase to low redshifts, more in concert with the QGs.

Pandya et al. (2017) showed that (fast-quenching) PSBs are more common at high redshifts relative to the (slow-quenching)
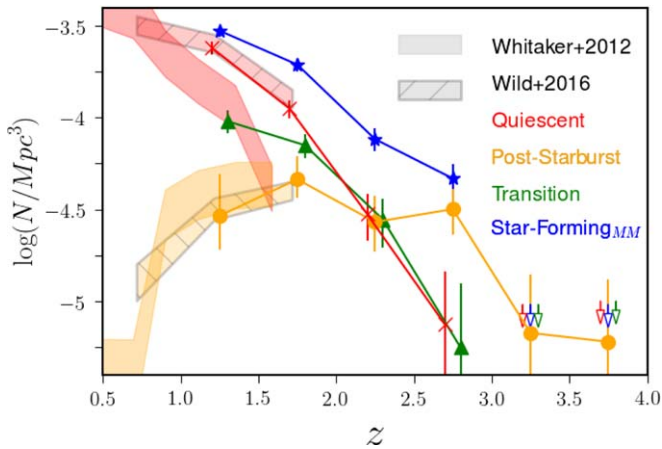
Figure 12. Comoving number densities of QGs (red), PSBs (orange), TGs (green), and mass-matched SFGs (blue) against redshift. Our results are consistent with the results from Wild et al. (2016), shown as hatched shaded regions. Results from NMBS (Whitaker et al. 2012a) are shown as non-hatched shaded regions. Notably, the shapes of the TG and QG curves appear quite similar, which is suggestive of them being along a similar evolutionary pathway. While both these tracks flatten out toward lower redshifts, the PSBs show strong evidence for a turnover around $z \sim 1.5$.

TGs that dominate the quenching process below $z \sim 0.7$, in qualitative agreement with Pacifici et al. (2016). This is as expected, since the young age of the universe at higher redshifts prohibits any long-timescale quenching from completing. Our results are consistent with this picture, where we find spatial number densities of TGs increasing sharply with decreasing redshift, while PSBs appear to have a turnover at $z \sim 1.5$.

As a short additional calculation, we use Equation (3) from Pandya et al. (2017),

$$\langle t_{\mathrm{TG}} \rangle_{z1,z2} = \langle n_{\mathrm{TG}} \rangle_{z_1,z_2} \times \left(\frac{dn_{\mathrm{QG}}}{dt} \right)^{-1}_{z_1,z_2}, \qquad (8)$$

to calculate average transition time for a galaxy based on number densities of TGs and QGs at varying redshifts. We find average transition timescales of $t_{\mathrm{TG}} \sim 1.63$ Gyr at $z = 1.5$ and $t_{\mathrm{TG}} \sim 0.95$ Gyr at $z = 2.5$, in rough agreement with Pandya et al. (2017) and slightly longer than the timescale of 1.24 Gyr from $z \sim 1.5$ clusters found in Foltz et al. (2018). We thus conclude that the vast majority of the TGs in our sample are in fact moving from the blue, disk-dominated, star-forming cloud to the red, bulge-dominated, quenched sequence, possibly through multiple mechanisms with similar timescales on the order of 1–2 Gyr.

8. Conclusions

In this work we have categorized ~ 7000 galaxies from ZFOURGE based on UV to near-IR rest-frame colors and spectral feature similarities. Building composite SEDs allowed us to leverage the large amount of multiwavelength photometry and accurate photometric redshifts from ZFOURGE for galaxies across a broad redshift range, $1 < z < 4$. These composite SEDs show a wide range of properties and independently yield expected relations based on emission-line EWs, sizes, masses, and number densities. Building composite SEDs also aided in the identification of rare populations in our sample, as well as

characterization of properties that are not typically available with photometry alone.

Additionally, we find evidence for galaxies with at least two quenching patterns. Most of these TGs show Hα emission with EW$_{\mathrm{REST}} \sim 40$ Å, SFRs ~ 1.5 dex beneath the star formation stellar mass relation, effective radii half that of SFGs of similar mass, Sérsic indices of 2–3 increasing with mass, and colors that lie on the boundary between QGs and SFGs on the UVJ diagram. The majority of these TGs have masses $10 < \log_{10}(M/M_\odot) < 11$. The other class of these galaxies is consistent with the classical "post-starburst" regime, showing small, bulge-dominated morphologies more consistent with QGs ($n \sim 3$–4), no nebular emission, and sSFRs just above the quiescent regime, but also bluer (V–J) colors than QGs and TGs at similar masses and redshifts.

The greater and increasing number density of the TGs at low redshifts (0.5 dex larger than PSBs at $z = 1.25$) implies that this group/quenching pathway is becoming more common, while the PSBs are becoming rarer at $z < 1.5$. This is potentially due to a longer timescale associated with said pathway, on the order of 1.5 Gyr, a factor of 1.5–7 times longer than the post-starburst phase is expected to last, and which cannot have occurred before $z \sim 4$.

The process that brings SFGs into the green valley creates changes in galaxy color, sSFR, size, and Sérsic index. The morphologies of galaxies appear, on average, to begin evolution toward higher Sérsic index before star formation ceases. Whether this morphological evolution leads directly to star formation turning off or there is a common cause of both changes remains unclear, but the observations are consistent with morphological quenching.

Appendix

In this appendix we present the composite SEDs and their associated properties. The composite SEDs and filter curves are available for download on Github.[12] We first list the properties derived from the composite SEDs themselves, such as EWs and UV slopes in Table 2 (Table 3) for the $1 < z < 3$ ($2.5 < z < 4$) composite SEDs.

Next are the parameters derived for individual galaxies that make up a composite SED, for which the medians, 16th percentile, and 84th percentile are given. In the case of morphological parameters, median absolute deviations are provided, to minimize errors due to resolution limits. These are given in Table 4 (Table 5).

---

[12] https://github.com/b4forrest/CompositeSEDs

Table 2
Parameters Derived from Composite SEDs at $1.0 < z < 3.0$

Composite ID	Class	$N_{\rm gal}$	$EW_{\rm [O~III]+H\beta}$ (Å)	$EW_{\rm H\alpha+[N~II]}$ (Å)	$D(4000)$	β
0	ELG	14	1170^{+40}_{-40}	1215^{+88}_{-88}	$0.90^{+0.01}_{-0.01}$	$-2.35^{+0.04}_{-0.04}$
1	SFG	323	265^{+11}_{-11}	277^{+20}_{-22}	$1.06^{+0.01}_{-0.01}$	$-2.00^{+0.02}_{-0.02}$
2	ELG	22	461^{+14}_{-14}	282^{+28}_{-29}	$1.10^{+0.01}_{-0.01}$	$-1.95^{+0.05}_{-0.05}$
3	SFG	62	102^{+12}_{-11}	183^{+21}_{-22}	$1.13^{+0.03}_{-0.03}$	$-1.87^{+0.03}_{-0.03}$
4	SFG	577	159^{+13}_{-12}	224^{+28}_{-29}	$1.14^{+0.02}_{-0.02}$	$-1.85^{+0.03}_{-0.03}$
5	SFG	537	132^{+35}_{-14}	188^{+35}_{-36}	$1.16^{+0.01}_{-0.01}$	$-1.75^{+0.03}_{-0.03}$
6	SFG	60	36^{+10}_{-10}	111^{+25}_{-26}	$1.27^{+0.03}_{-0.03}$	$-1.74^{+0.03}_{-0.03}$
7	SFG	28	135^{+34}_{-14}	233^{+34}_{-35}	$1.14^{+0.06}_{-0.07}$	$-1.72^{+0.03}_{-0.03}$
8	SFG	51	81^{+13}_{-10}	121^{+13}_{-16}	$1.17^{+0.01}_{-0.02}$	$-1.67^{+0.05}_{-0.05}$
9	SFG	34	227^{+23}_{-23}	254^{+64}_{-64}	$1.19^{+0.01}_{-0.01}$	$-1.67^{+0.05}_{-0.05}$
10	SFG	610	102^{+10}_{-10}	178^{+15}_{-17}	$1.19^{+0.01}_{-0.02}$	$-1.60^{+0.04}_{-0.04}$
11	SFG	419	88^{+11}_{-11}	202^{+21}_{-23}	$1.20^{+0.03}_{-0.03}$	$-1.54^{+0.04}_{-0.04}$
12	SFG	503	79^{+12}_{-12}	173^{+28}_{-29}	$1.21^{+0.03}_{-0.04}$	$-1.53^{+0.04}_{-0.04}$
13	SFG	134	39^{+10}_{-10}	124^{+15}_{-17}	$1.26^{+0.00}_{-0.00}$	$-1.50^{+0.05}_{-0.05}$
14	SFG	37	37^{+20}_{-20}	135^{+65}_{-65}	$1.31^{+0.01}_{-0.01}$	$-1.45^{+0.07}_{-0.07}$
15	SFG	61	20^{+10}_{-10}	126^{+15}_{-17}	$1.29^{+0.04}_{-0.05}$	$-1.40^{+0.07}_{-0.07}$
16	SFG	41	24^{+15}_{-15}	147^{+40}_{-41}	$1.29^{+0.06}_{-0.07}$	$-1.40^{+0.08}_{-0.08}$
17	SFG	241	82^{+10}_{-15}	164^{+13}_{-15}	$1.22^{+0.01}_{-0.01}$	$-1.39^{+0.04}_{-0.04}$
18	SFG	71	38^{+13}_{-12}	130^{+54}_{-55}	$1.27^{+0.04}_{-0.04}$	$-1.38^{+0.06}_{-0.06}$
19	SFG	31	17^{+10}_{-10}	130^{+13}_{-16}	$1.33^{+0.02}_{-0.02}$	$-1.37^{+0.08}_{-0.08}$
20	SFG	20	14^{+12}_{-11}	72^{+24}_{-26}	$1.40^{+0.04}_{-0.05}$	$-1.37^{+0.09}_{-0.09}$
21	SFG	145	50^{+14}_{-13}	142^{+39}_{-40}	$1.27^{+0.05}_{-0.06}$	$-1.33^{+0.06}_{-0.06}$
22	SFG	60	26^{+13}_{-10}	137^{+13}_{-16}	$1.30^{+0.01}_{-0.02}$	$-1.32^{+0.07}_{-0.07}$
23	SFG	132	101^{+10}_{-10}	199^{+36}_{-37}	$1.21^{+0.03}_{-0.04}$	$-1.32^{+0.05}_{-0.05}$
24	SFG	107	40^{+31}_{-12}	128^{+31}_{-32}	$1.29^{+0.02}_{-0.03}$	$-1.30^{+0.07}_{-0.07}$
25	SFG	21	16^{+13}_{-13}	103^{+35}_{-37}	$1.52^{+0.02}_{-0.02}$	$-1.28^{+0.07}_{-0.07}$
26	SFG	97	61^{+37}_{-13}	146^{+37}_{-38}	$1.27^{+0.02}_{-0.02}$	$-1.27^{+0.05}_{-0.05}$
27	SFG	53	29^{+52}_{-17}	135^{+52}_{-53}	$1.35^{+0.03}_{-0.03}$	$-1.16^{+0.08}_{-0.08}$
28	SFG	24	2^{+19}_{-18}	89^{+74}_{-75}	$1.67^{+0.05}_{-0.07}$	$-1.16^{+0.41}_{-0.41}$
29	SFG	20	-17^{+12}_{-12}	95^{+26}_{-27}	$1.38^{+0.03}_{-0.03}$	$-1.15^{+0.10}_{-0.10}$
30	SFG	107	37^{+13}_{-13}	123^{+38}_{-39}	$1.31^{+0.05}_{-0.06}$	$-1.15^{+0.08}_{-0.08}$
31	SFG	24	46^{+17}_{-16}	118^{+44}_{-45}	$1.36^{+0.05}_{-0.06}$	$-1.13^{+0.13}_{-0.13}$
32	SFG	77	64^{+13}_{-13}	178^{+33}_{-34}	$1.25^{+0.02}_{-0.02}$	$-1.11^{+0.06}_{-0.06}$
33	SFG	25	-14^{+44}_{-44}	110^{+182}_{-182}	$1.40^{+0.02}_{-0.02}$	$-1.11^{+0.12}_{-0.12}$
34	SFG	46	18^{+10}_{-15}	113^{+13}_{-15}	$1.31^{+0.02}_{-0.02}$	$-1.11^{+0.07}_{-0.07}$
35	SFG	38	3^{+11}_{-11}	132^{+22}_{-23}	$1.37^{+0.02}_{-0.03}$	$-1.10^{+0.09}_{-0.09}$
36	SFG	66	75^{+14}_{-14}	137^{+31}_{-32}	$1.27^{+0.02}_{-0.02}$	$-1.10^{+0.05}_{-0.05}$
37	SFG	50	48^{+11}_{-10}	178^{+15}_{-17}	$1.29^{+0.01}_{-0.01}$	$-1.08^{+0.05}_{-0.05}$
38	SFG	30	13^{+13}_{-12}	100^{+26}_{-27}	$1.42^{+0.03}_{-0.03}$	$-0.99^{+0.10}_{-0.10}$
39	SFG	26	6^{+10}_{-10}	125^{+20}_{-22}	$1.37^{+0.01}_{-0.02}$	$-0.97^{+0.10}_{-0.10}$
40	TG	21	38^{+13}_{-10}	38^{+13}_{-16}	$1.62^{+0.00}_{-0.00}$	$-0.97^{+0.12}_{-0.12}$
41	SFG	27	65^{+18}_{-18}	275^{+17}_{-19}	$1.29^{+0.06}_{-0.07}$	$-0.97^{+0.10}_{-0.10}$
42	SFG	36	26^{+10}_{-9}	179^{+26}_{-28}	$1.26^{+0.01}_{-0.01}$	$-0.97^{+0.07}_{-0.07}$
43	SFG	52	69^{+14}_{-10}	139^{+14}_{-17}	$1.30^{+0.01}_{-0.01}$	$-0.96^{+0.07}_{-0.07}$
44	SFG	37	9^{+12}_{-12}	109^{+31}_{-32}	$1.37^{+0.02}_{-0.03}$	$-0.89^{+0.09}_{-0.09}$
45	SFG	21	71^{+31}_{-30}	177^{+121}_{-122}	$1.29^{+0.03}_{-0.03}$	$-0.87^{+0.09}_{-0.09}$
46	SFG	50	68^{+22}_{-22}	203^{+70}_{-70}	$1.28^{+0.04}_{-0.05}$	$-0.87^{+0.09}_{-0.09}$
47	SFG	54	16^{+17}_{-16}	112^{+56}_{-57}	$1.38^{+0.10}_{-0.11}$	$-0.86^{+0.06}_{-0.06}$
48	SFG	47	33^{+20}_{-20}	106^{+69}_{-69}	$1.43^{+0.01}_{-0.02}$	$-0.70^{+0.13}_{-0.13}$
49	SFG	28	1^{+19}_{-19}	90^{+52}_{-53}	$1.50^{+0.00}_{-0.00}$	$-0.69^{+0.23}_{-0.23}$
50	SFG	26	7^{+15}_{-14}	49^{+36}_{-37}	$1.39^{+0.01}_{-0.01}$	$-0.63^{+0.08}_{-0.08}$
51	SFG	30	25^{+12}_{-11}	87^{+30}_{-31}	$1.45^{+0.07}_{-0.09}$	$-0.55^{+0.12}_{-0.12}$
52	TG	29	14^{+19}_{-18}	39^{+52}_{-52}	$1.59^{+0.05}_{-0.06}$	$-0.39^{+0.11}_{-0.11}$
53	SFG	35	-19^{+10}_{-10}	60^{+27}_{-28}	$1.51^{+0.03}_{-0.03}$	$-0.38^{+0.26}_{-0.26}$
54	TG	38	39^{+11}_{-10}	46^{+19}_{-20}	$1.50^{+0.10}_{-0.13}$	$-0.38^{+0.12}_{-0.12}$
55	SFG	29	-11^{+17}_{-17}	92^{+68}_{-68}	$1.48^{+0.10}_{-0.12}$	$-0.35^{+0.27}_{-0.27}$
56	SFG	28	16^{+23}_{-23}	89^{+75}_{-75}	$1.49^{+0.09}_{-0.11}$	$-0.34^{+0.11}_{-0.11}$
57	SFG	20	2^{+15}_{-15}	30^{+38}_{-38}	$1.60^{+0.08}_{-0.08}$	$-0.30^{+0.26}_{-0.26}$

Table 2
(Continued)

Composite ID	Class	$N_{\rm gal}$	EW$_{\rm [O\,III]+H\beta}$ (Å)	EW$_{\rm H\alpha+[N\,II]}$ (Å)	$D(4000)$	β
58	SFG	32	-24^{+20}_{-20}	58^{+68}_{-68}	$1.44^{+0.04}_{-0.04}$	$-0.23^{+0.16}_{-0.16}$
59	TG	52	23^{+12}_{-12}	23^{+25}_{-26}	$1.70^{+0.04}_{-0.05}$	$-0.23^{+0.12}_{-0.12}$
60	SFG	27	-4^{+52}_{-33}	71^{+52}_{-53}	$1.51^{+0.03}_{-0.04}$	$-0.18^{+0.17}_{-0.17}$
61	TG	30	43^{+23}_{-11}	50^{+23}_{-24}	$1.62^{+0.03}_{-0.04}$	$0.06^{+0.24}_{-0.24}$
62	SFG	33	21^{+14}_{-14}	100^{+29}_{-31}	$1.60^{+0.03}_{-0.03}$	$0.26^{+0.23}_{-0.23}$
63	TG	20	47^{+17}_{-17}	56^{+56}_{-57}	$1.52^{+0.02}_{-0.02}$	$0.58^{+0.22}_{-0.22}$
64	QG	31	15^{+11}_{-11}	1^{+22}_{-24}	$1.84^{+0.10}_{-0.11}$	$0.67^{+0.32}_{-0.32}$
65	PSB	58	1^{+14}_{-14}	1^{+37}_{-38}	$1.69^{+0.08}_{-0.10}$	$1.03^{+0.17}_{-0.17}$
66	QG	70	10^{+11}_{-11}	2^{+28}_{-29}	$1.77^{+0.08}_{-0.10}$	$1.04^{+0.22}_{-0.22}$
67	SFG	25	12^{+11}_{-11}	93^{+22}_{-23}	$1.64^{+0.04}_{-0.05}$	$1.04^{+0.26}_{-0.26}$
68	QG	82	-4^{+11}_{-11}	-11^{+24}_{-25}	$1.84^{+0.07}_{-0.09}$	$1.13^{+0.48}_{-0.48}$
69	PSB	59	-35^{+10}_{-10}	-27^{+16}_{-18}	$1.73^{+0.08}_{-0.08}$	$1.29^{+0.16}_{-0.16}$
70	QG	67	-4^{+10}_{-10}	5^{+13}_{-16}	$1.75^{+0.11}_{-0.14}$	$1.39^{+0.20}_{-0.20}$
71	QG	110	13^{+10}_{-10}	2^{+14}_{-17}	$1.78^{+0.02}_{-0.03}$	$1.45^{+0.21}_{-0.21}$

Table 3
Parameters Derived from Composite SEDs at $2.5 < z < 4.0$

Composite ID	Class	$N_{\rm gal}$	EW$_{\rm [O\,III]+H\beta}$ (Å)	$D(4000)$	β
0	ELG	19	2578^{+78}_{-89}	$0.91^{+0.00}_{-0.00}$	$-2.05^{+0.07}_{-0.07}$
1	ELG	64	755^{+5}_{-14}	$0.94^{+0.08}_{-0.10}$	$-2.00^{+0.04}_{-0.04}$
2	SFG	52	336^{+10}_{-11}	$1.16^{+0.04}_{-0.04}$	$-1.91^{+0.03}_{-0.03}$
3	ELG	22	599^{+5}_{-5}	$0.95^{+0.09}_{-0.11}$	$-1.87^{+0.13}_{-0.13}$
4	SFG	89	355^{+7}_{-8}	$1.17^{+0.03}_{-0.03}$	$-1.80^{+0.03}_{-0.03}$
5	SFG	88	224^{+10}_{-16}	$1.17^{+0.00}_{-0.00}$	$-1.69^{+0.03}_{-0.03}$
6	SFG	48	315^{+7}_{-8}	$1.17^{+0.05}_{-0.06}$	$-1.66^{+0.05}_{-0.05}$
7	SFG	37	148^{+9}_{-15}	$1.23^{+0.01}_{-0.01}$	$-1.56^{+0.05}_{-0.05}$
8	SFG	167	180^{+9}_{-10}	$1.19^{+0.02}_{-0.02}$	$-1.52^{+0.03}_{-0.03}$
9	SFG	27	100^{+10}_{-10}	$1.18^{+0.04}_{-0.04}$	$-1.49^{+0.06}_{-0.06}$
10	SFG	135	149^{+11}_{-17}	$1.24^{+0.00}_{-0.00}$	$-1.35^{+0.04}_{-0.04}$
11	SFG	76	76^{+10}_{-14}	$1.23^{+0.00}_{-0.00}$	$-1.25^{+0.04}_{-0.04}$
12	SFG	20	1^{+10}_{-11}	$1.24^{+0.06}_{-0.06}$	$-1.20^{+0.08}_{-0.08}$
13	SFG	39	89^{+9}_{-9}	$1.24^{+0.01}_{-0.01}$	$-1.11^{+0.05}_{-0.05}$
14	SFG	39	77^{+10}_{-11}	$1.28^{+0.00}_{-0.00}$	$-0.96^{+0.07}_{-0.07}$
15	SFG	22	57^{+8}_{-10}	$1.29^{+0.03}_{-0.03}$	$-0.93^{+0.13}_{-0.13}$
16	SFG	19	18^{+11}_{-13}	$1.53^{+0.10}_{-0.11}$	$-0.70^{+0.42}_{-0.42}$
17	SFG	30	27^{+12}_{-16}	$1.36^{+0.02}_{-0.02}$	$-0.51^{+0.13}_{-0.13}$
18	PSB	16	38^{+10}_{-12}	$1.60^{+0.18}_{-0.24}$	$-0.14^{+0.24}_{-0.24}$
19	PSB	28	-21^{+10}_{-11}	$1.71^{+0.09}_{-0.09}$	$0.49^{+0.28}_{-0.28}$

Table 4
Analog Galaxy Parameters for Composite SEDs at $1.0 < z < 3.0$

Composite ID	Class	$\log_{10}(M/M_\odot)$	sSFR (yr^{-1})	A_V (mag)	$(V–J)$	$(U–V)$	r_e (kpc)	n
0	ELG	$8.36^{+0.25}_{-0.23}$	$-7.00^{+0.03}_{-0.08}$	$0.40^{+0.10}_{-0.10}$	$-0.78^{+0.13}_{-0.08}$	$0.26^{+0.10}_{-0.05}$	0.8 ± 0.3	2.8 ± 1.9
1	SFG	$9.09^{+0.35}_{-0.45}$	$-8.35^{+1.11}_{-0.37}$	$0.30^{+0.30}_{-0.30}$	$0.07^{+0.18}_{-0.25}$	$0.30^{+0.08}_{-0.08}$	1.7 ± 0.6	1.3 ± 0.6
2	ELG	$8.79^{+0.40}_{-0.27}$	$-7.95^{+0.87}_{-0.93}$	$0.65^{+0.26}_{-0.55}$	$0.08^{+0.26}_{-0.40}$	$0.46^{+0.08}_{-0.08}$	1.5 ± 0.6	1.4 ± 0.9
3	SFG	$9.22^{+0.31}_{-0.38}$	$-8.72^{+0.24}_{-0.27}$	$0.20^{+0.10}_{-0.12}$	$0.25^{+0.10}_{-0.16}$	$0.39^{+0.07}_{-0.05}$	1.9 ± 0.6	1.2 ± 0.5
4	SFG	$9.27^{+0.31}_{-0.32}$	$-8.68^{+0.38}_{-0.32}$	$0.30^{+0.20}_{-0.20}$	$0.20^{+0.15}_{-0.18}$	$0.43^{+0.07}_{-0.07}$	2.0 ± 0.7	1.1 ± 0.5
5	SFG	$9.35^{+0.27}_{-0.35}$	$-8.83^{+0.34}_{-0.21}$	$0.30^{+0.20}_{-0.20}$	$0.26^{+0.12}_{-0.16}$	$0.52^{+0.06}_{-0.07}$	2.2 ± 0.7	1.2 ± 0.5
6	SFG	$9.54^{+0.36}_{-0.24}$	$-9.02^{+0.58}_{-0.24}$	$0.55^{+0.41}_{-0.25}$	$0.72^{+0.15}_{-0.10}$	$0.71^{+0.07}_{-0.08}$	2.8 ± 1.2	1.0 ± 0.5
7	SFG	$9.38^{+0.56}_{-0.24}$	$-8.80^{+0.64}_{-0.40}$	$0.70^{+0.30}_{-0.40}$	$0.72^{+0.15}_{-0.10}$	$0.62^{+0.05}_{-0.11}$	2.4 ± 0.7	1.2 ± 0.6
8	SFG	$9.33^{+0.33}_{-0.40}$	$-8.79^{+0.31}_{-0.41}$	$0.60^{+0.10}_{-0.40}$	$0.52^{+0.16}_{-0.11}$	$0.57^{+0.07}_{-0.09}$	2.1 ± 0.5	0.9 ± 0.4
9	SFG	$9.16^{+0.27}_{-0.23}$	$-8.93^{+0.44}_{-0.29}$	$0.40^{+0.32}_{-0.30}$	$0.24^{+0.15}_{-0.12}$	$0.59^{+0.07}_{-0.06}$	1.5 ± 0.6	1.9 ± 0.9
10	SFG	$9.48^{+0.27}_{-0.31}$	$-8.90^{+0.26}_{-0.30}$	$0.40^{+0.20}_{-0.20}$	$0.34^{+0.13}_{-0.15}$	$0.57^{+0.07}_{-0.07}$	2.3 ± 0.9	1.2 ± 0.5
11	SFG	$9.54^{+0.27}_{-0.34}$	$-8.98^{+0.32}_{-0.22}$	$0.50^{+0.20}_{-0.30}$	$0.42^{+0.11}_{-0.15}$	$0.64^{+0.07}_{-0.08}$	2.4 ± 0.9	1.3 ± 0.5
12	SFG	$9.58^{+0.33}_{-0.39}$	$-9.00^{+0.28}_{-0.23}$	$0.50^{+0.30}_{-0.20}$	$0.48^{+0.12}_{-0.15}$	$0.69^{+0.06}_{-0.06}$	2.5 ± 0.9	1.2 ± 0.5
13	SFG	$9.66^{+0.28}_{-0.26}$	$-8.99^{+0.35}_{-0.22}$	$0.80^{+0.20}_{-0.30}$	$0.70^{+0.11}_{-0.09}$	$0.77^{+0.07}_{-0.07}$	2.8 ± 1.1	1.0 ± 0.4
14	SFG	$9.70^{+0.27}_{-0.32}$	$-9.21^{+0.31}_{-0.43}$	$0.60^{+0.40}_{-0.40}$	$0.73^{+0.11}_{-0.11}$	$0.97^{+0.05}_{-0.08}$	2.8 ± 1.4	1.5 ± 0.6
15	SFG	$9.87^{+0.32}_{-0.28}$	$-8.99^{+0.27}_{-0.21}$	$0.90^{+0.24}_{-0.30}$	$0.82^{+0.08}_{-0.07}$	$0.89^{+0.05}_{-0.08}$	2.8 ± 0.8	1.0 ± 0.5
16	SFG	$10.02^{+0.38}_{-0.42}$	$-8.91^{+0.34}_{-0.28}$	$1.00^{+0.30}_{-0.20}$	$1.02^{+0.07}_{-0.13}$	$0.86^{+0.05}_{-0.07}$	3.3 ± 1.2	0.9 ± 0.5
17	SFG	$9.64^{+0.34}_{-0.30}$	$-9.00^{+0.23}_{-0.40}$	$0.70^{+0.30}_{-0.30}$	$0.53^{+0.11}_{-0.14}$	$0.75^{+0.06}_{-0.08}$	2.4 ± 1.0	1.4 ± 0.6
18	SFG	$9.88^{+0.26}_{-0.40}$	$-8.99^{+0.31}_{-0.21}$	$0.80^{+0.30}_{-0.20}$	$0.83^{+0.11}_{-0.09}$	$0.82^{+0.06}_{-0.06}$	3.4 ± 1.2	1.0 ± 0.4
19	SFG	$10.22^{+0.26}_{-0.58}$	$-9.12^{+0.50}_{-0.23}$	$1.10^{+0.42}_{-0.20}$	$1.17^{+0.12}_{-0.05}$	$0.99^{+0.07}_{-0.08}$	4.0 ± 0.9	0.7 ± 0.2
20	SFG	$9.79^{+0.35}_{-0.45}$	$-9.41^{+0.20}_{-0.33}$	$0.60^{+0.20}_{-0.40}$	$0.78^{+0.05}_{-0.05}$	$1.06^{+0.06}_{-0.04}$	2.2 ± 0.5	1.6 ± 0.7
21	SFG	$9.79^{+0.28}_{-0.35}$	$-8.99^{+0.27}_{-0.22}$	$0.90^{+0.10}_{-0.30}$	$0.68^{+0.10}_{-0.10}$	$0.83^{+0.06}_{-0.07}$	2.9 ± 1.0	1.1 ± 0.4
22	SFG	$10.00^{+0.35}_{-0.34}$	$-8.99^{+0.21}_{-0.25}$	$1.15^{+0.15}_{-0.25}$	$0.99^{+0.07}_{-0.06}$	$0.96^{+0.05}_{-0.08}$	3.4 ± 0.9	1.1 ± 0.4
23	SFG	$9.70^{+0.27}_{-0.37}$	$-9.17^{+0.27}_{-0.37}$	$0.50^{+0.20}_{-0.20}$	$0.38^{+0.11}_{-0.12}$	$0.68^{+0.05}_{-0.07}$	2.2 ± 0.8	1.3 ± 0.5
24	SFG	$9.96^{+0.30}_{-0.37}$	$-9.00^{+0.19}_{-0.23}$	$1.00^{+0.20}_{-0.30}$	$0.84^{+0.09}_{-0.09}$	$0.93^{+0.06}_{-0.06}$	3.3 ± 1.2	1.2 ± 0.6
25	SFG	$10.19^{+0.43}_{-0.62}$	$-9.93^{+0.37}_{-0.18}$	$0.60^{+0.58}_{-0.30}$	$0.99^{+0.08}_{-0.07}$	$1.33^{+0.06}_{-0.05}$	1.8 ± 0.9	2.4 ± 0.7
26	SFG	$9.81^{+0.28}_{-0.42}$	$-9.17^{+0.36}_{-0.43}$	$0.70^{+0.20}_{-0.20}$	$0.57^{+0.10}_{-0.14}$	$0.75^{+0.07}_{-0.06}$	2.4 ± 0.7	1.3 ± 0.6
27	SFG	$10.27^{+0.22}_{-0.42}$	$-9.20^{+0.27}_{-0.44}$	$1.40^{+0.20}_{-0.40}$	$1.08^{+0.08}_{-0.06}$	$1.14^{+0.06}_{-0.06}$	3.4 ± 0.9	0.9 ± 0.4
28	SFG	$10.71^{+0.31}_{-0.33}$	$-10.36^{+0.31}_{-1.56}$	$1.75^{+0.85}_{-0.25}$	$1.88^{+0.12}_{-0.06}$	$2.01^{+0.14}_{-0.09}$	3.4 ± 0.8	1.4 ± 0.6
29	SFG	$10.39^{+0.33}_{-0.47}$	$-9.28^{+0.29}_{-0.18}$	$1.30^{+0.40}_{-0.20}$	$1.36^{+0.04}_{-0.04}$	$1.20^{+0.03}_{-0.10}$	3.6 ± 1.4	0.8 ± 0.2
30	SFG	$10.03^{+0.31}_{-0.42}$	$-9.04^{+0.20}_{-0.40}$	$1.10^{+0.20}_{-0.30}$	$0.93^{+0.07}_{-0.10}$	$1.02^{+0.05}_{-0.06}$	3.1 ± 1.3	1.1 ± 0.6
31	SFG	$10.01^{+0.36}_{-0.30}$	$-9.36^{+0.30}_{-0.29}$	$1.20^{+0.20}_{-0.40}$	$0.92^{+0.05}_{-0.09}$	$1.15^{+0.02}_{-0.05}$	2.2 ± 0.8	1.2 ± 0.4
32	SFG	$9.89^{+0.33}_{-0.37}$	$-9.08^{+0.18}_{-0.36}$	$0.90^{+0.20}_{-0.20}$	$0.65^{+0.10}_{-0.13}$	$0.85^{+0.06}_{-0.06}$	2.6 ± 0.9	1.1 ± 0.5
33	SFG	$10.26^{+0.29}_{-0.42}$	$-9.19^{+0.40}_{-0.45}$	$1.70^{+0.20}_{-0.33}$	$1.36^{+0.10}_{-0.04}$	$1.22^{+0.09}_{-0.04}$	3.5 ± 0.8	0.9 ± 0.3
34	SFG	$10.11^{+0.27}_{-0.40}$	$-9.09^{+0.28}_{-0.29}$	$1.30^{+0.18}_{-0.30}$	$1.04^{+0.08}_{-0.05}$	$1.02^{+0.05}_{-0.09}$	3.6 ± 0.8	0.9 ± 0.5
35	SFG	$10.06^{+0.50}_{-0.33}$	$-9.09^{+0.31}_{-0.32}$	$1.55^{+0.15}_{-0.45}$	$1.25^{+0.08}_{-0.09}$	$1.13^{+0.08}_{-0.07}$	3.6 ± 1.0	0.9 ± 0.3
36	SFG	$9.73^{+0.42}_{-0.40}$	$-9.36^{+0.36}_{-0.79}$	$0.60^{+0.20}_{-0.10}$	$0.48^{+0.11}_{-0.11}$	$0.77^{+0.07}_{-0.08}$	2.3 ± 0.8	1.4 ± 0.5
37	SFG	$9.91^{+0.38}_{-0.48}$	$-9.36^{+0.33}_{-0.41}$	$0.80^{+0.20}_{-0.22}$	$0.60^{+0.08}_{-0.08}$	$0.89^{+0.07}_{-0.06}$	2.4 ± 0.9	1.6 ± 0.7
38	SFG	$10.45^{+0.33}_{-0.45}$	$-9.18^{+0.37}_{-0.30}$	$1.65^{+0.35}_{-0.35}$	$1.41^{+0.07}_{-0.07}$	$1.32^{+0.06}_{-0.06}$	3.7 ± 1.1	1.1 ± 0.5
39	SFG	$10.29^{+0.32}_{-0.41}$	$-9.12^{+0.34}_{-0.28}$	$1.55^{+0.25}_{-0.45}$	$1.27^{+0.08}_{-0.07}$	$1.12^{+0.09}_{-0.05}$	3.3 ± 0.5	0.8 ± 0.1
40	TG	$10.51^{+0.58}_{-0.40}$	$-10.09^{+0.17}_{-0.63}$	$0.70^{+0.38}_{-0.50}$	$1.19^{+0.05}_{-0.05}$	$1.60^{+0.07}_{-0.07}$	2.2 ± 1.1	4.6 ± 2.4
41	SFG	$10.02^{+0.36}_{-0.40}$	$-9.17^{+0.26}_{-1.05}$	$1.30^{+0.10}_{-0.20}$	$0.96^{+0.04}_{-0.06}$	$1.05^{+0.05}_{-0.06}$	2.7 ± 1.2	1.4 ± 0.6
42	SFG	$10.00^{+0.29}_{-0.28}$	$-9.00^{+0.34}_{-0.77}$	$1.10^{+0.20}_{-0.10}$	$0.83^{+0.08}_{-0.08}$	$0.89^{+0.03}_{-0.06}$	2.9 ± 1.0	0.8 ± 0.3
43	SFG	$9.92^{+0.22}_{-0.33}$	$-9.20^{+0.20}_{-0.52}$	$0.90^{+0.20}_{-0.20}$	$0.74^{+0.10}_{-0.06}$	$0.97^{+0.05}_{-0.09}$	2.7 ± 1.2	1.5 ± 0.7
44	SFG	$10.10^{+0.57}_{-0.44}$	$-9.44^{+0.46}_{-0.44}$	$1.40^{+0.20}_{-0.60}$	$1.08^{+0.09}_{-0.05}$	$1.20^{+0.08}_{-0.06}$	2.7 ± 0.9	0.9 ± 0.3
45	SFG	$9.67^{+0.51}_{-0.47}$	$-10.46^{+0.95}_{-1.80}$	$0.70^{+0.10}_{-0.28}$	$0.46^{+0.09}_{-0.15}$	$0.82^{+0.05}_{-0.06}$	2.1 ± 0.7	2.6 ± 0.9
46	SFG	$10.05^{+0.26}_{-0.44}$	$-9.36^{+0.36}_{-0.63}$	$1.20^{+0.10}_{-0.20}$	$0.85^{+0.08}_{-0.12}$	$1.01^{+0.07}_{-0.03}$	2.5 ± 0.8	1.2 ± 0.5
47	SFG	$10.32^{+0.34}_{-0.35}$	$-9.23^{+0.24}_{-0.53}$	$1.60^{+0.20}_{-0.40}$	$1.26^{+0.05}_{-0.08}$	$1.28^{+0.05}_{-0.06}$	3.0 ± 1.3	1.3 ± 0.7
48	SFG	$10.43^{+0.38}_{-0.40}$	$-9.58^{+0.39}_{-0.71}$	$1.60^{+0.30}_{-0.60}$	$1.28^{+0.09}_{-0.07}$	$1.39^{+0.09}_{-0.06}$	2.8 ± 0.8	1.6 ± 0.6
49	SFG	$10.59^{+0.38}_{-0.19}$	$-9.17^{+0.39}_{-0.44}$	$2.60^{+0.17}_{-0.60}$	$1.92^{+0.07}_{-0.04}$	$1.61^{+0.09}_{-0.09}$	4.5 ± 0.9	0.8 ± 0.3
50	SFG	$9.95^{+0.49}_{-0.48}$	$-9.58^{+0.39}_{-0.88}$	$1.40^{+0.10}_{-0.60}$	$0.99^{+0.07}_{-0.16}$	$1.22^{+0.10}_{-0.05}$	2.0 ± 1.0	2.1 ± 0.7
51	SFG	$10.36^{+0.43}_{-0.58}$	$-9.58^{+0.21}_{-1.59}$	$1.50^{+0.20}_{-0.30}$	$1.10^{+0.08}_{-0.06}$	$1.33^{+0.07}_{-0.05}$	2.4 ± 0.9	2.1 ± 0.8
52	TG	$10.23^{+0.35}_{-0.57}$	$-10.36^{+0.60}_{-0.32}$	$0.80^{+0.60}_{-0.55}$	$1.00^{+0.04}_{-0.05}$	$1.44^{+0.06}_{-0.05}$	1.3 ± 0.6	3.7 ± 2.4
53	SFG	$10.70^{+0.28}_{-0.32}$	$-9.74^{+0.10}_{-1.12}$	$2.80^{+0.10}_{-0.66}$	$1.99^{+0.07}_{-0.06}$	$1.76^{+0.09}_{-0.07}$	3.8 ± 0.8	1.2 ± 0.4
54	TG	$10.41^{+0.37}_{-0.42}$	$-10.15^{+0.24}_{-0.40}$	$1.00^{+0.50}_{-0.71}$	$1.12^{+0.06}_{-0.08}$	$1.52^{+0.05}_{-0.07}$	2.3 ± 1.0	3.0 ± 1.0
55	SFG	$10.79^{+0.35}_{-0.32}$	$-9.77^{+0.49}_{-0.61}$	$2.90^{+0.30}_{-0.60}$	$2.18^{+0.14}_{-0.06}$	$1.88^{+0.13}_{-0.10}$	4.1 ± 0.9	1.3 ± 0.4
56	TG	$10.57^{+0.26}_{-0.35}$	$-9.84^{+0.43}_{-0.38}$	$1.45^{+0.62}_{-0.62}$	$1.41^{+0.09}_{-0.07}$	$1.56^{+0.05}_{-0.09}$	3.4 ± 1.3	2.0 ± 0.5
57	SFG	$10.64^{+0.25}_{-0.18}$	$-9.84^{+0.39}_{-0.86}$	$1.90^{+0.50}_{-0.70}$	$1.64^{+0.04}_{-0.09}$	$1.74^{+0.04}_{-0.09}$	3.9 ± 1.5	1.7 ± 0.7

Table 4
(Continued)

Composite ID	Class	$\log_{10}(M/M_\odot)$	sSFR (yr^{-1})	A_V (mag)	(V–J)	(U–V)	r_e (kpc)	n
58	SFG	$10.37^{+0.43}_{-0.30}$	$-9.45^{+0.45}_{-0.33}$	$2.00^{+0.10}_{-0.70}$	$1.48^{+0.05}_{-0.04}$	$1.43^{+0.08}_{-0.05}$	3.3 ± 1.4	1.1 ± 0.4
59	TG	$10.51^{+0.41}_{-0.37}$	$-10.70^{+0.34}_{-0.38}$	$0.40^{+0.40}_{-0.30}$	$1.08^{+0.10}_{-0.04}$	$1.65^{+0.08}_{-0.06}$	1.7 ± 1.0	4.7 ± 1.7
60	SFG	$10.50^{+0.31}_{-0.23}$	$-9.56^{+0.28}_{-1.74}$	$2.00^{+0.30}_{-0.30}$	$1.54^{+0.08}_{-0.05}$	$1.56^{+0.10}_{-0.07}$	4.3 ± 1.6	1.6 ± 0.6
61	TG	$10.64^{+0.19}_{-0.46}$	$-10.41^{+0.52}_{-0.37}$	$0.85^{+0.52}_{-0.19}$	$1.27^{+0.04}_{-0.06}$	$1.68^{+0.05}_{-0.07}$	2.1 ± 0.8	2.2 ± 1.1
62	TG	$10.75^{+0.27}_{-0.33}$	$-10.15^{+0.43}_{-1.01}$	$2.10^{+0.39}_{-0.80}$	$1.75^{+0.07}_{-0.06}$	$1.84^{+0.09}_{-0.11}$	3.2 ± 1.1	1.3 ± 0.6
63	TG	$10.50^{+0.29}_{-0.57}$	$-10.91^{+0.75}_{-0.65}$	$0.95^{+0.45}_{-0.84}$	$1.08^{+0.05}_{-0.08}$	$1.52^{+0.05}_{-0.06}$	1.9 ± 0.6	3.5 ± 1.8
64	QG	$10.85^{+0.20}_{-0.54}$	$-11.08^{+0.54}_{-0.20}$	$0.80^{+0.62}_{-0.20}$	$1.48^{+0.06}_{-0.12}$	$2.01^{+0.10}_{-0.13}$	2.3 ± 0.7	2.9 ± 1.1
65	PSB	$10.52^{+0.34}_{-0.43}$	$-11.23^{+0.53}_{-1.78}$	$0.40^{+0.10}_{-0.20}$	$0.82^{+0.07}_{-0.11}$	$1.54^{+0.04}_{-0.04}$	0.9 ± 0.3	3.5 ± 1.1
66	QG	$10.57^{+0.38}_{-0.31}$	$-11.38^{+0.47}_{-1.60}$	$0.50^{+0.20}_{-0.20}$	$1.16^{+0.05}_{-0.04}$	$1.83^{+0.06}_{-0.06}$	1.7 ± 0.6	4.5 ± 1.3
67	TG	$10.51^{+0.42}_{-0.36}$	$-10.54^{+0.39}_{-3.10}$	$1.10^{+0.82}_{-0.22}$	$1.40^{+0.10}_{-0.06}$	$1.67^{+0.15}_{-0.06}$	2.8 ± 1.2	1.5 ± 0.7
68	QG	$10.68^{+0.27}_{-0.37}$	$-11.69^{+0.31}_{-1.55}$	$0.50^{+0.20}_{-0.30}$	$1.26^{+0.07}_{-0.06}$	$1.91^{+0.06}_{-0.05}$	1.7 ± 0.6	3.5 ± 1.1
69	PSB	$10.51^{+0.32}_{-0.35}$	$-11.38^{+0.62}_{-4.10}$	$0.50^{+0.17}_{-0.40}$	$0.93^{+0.09}_{-0.06}$	$1.60^{+0.05}_{-0.04}$	1.1 ± 0.4	3.6 ± 1.1
70	QG	$10.37^{+0.47}_{-0.43}$	$-11.38^{+0.15}_{-5.47}$	$0.30^{+0.44}_{-0.10}$	$1.00^{+0.05}_{-0.05}$	$1.69^{+0.07}_{-0.04}$	1.3 ± 0.4	3.7 ± 0.9
71	QG	$10.57^{+0.31}_{-0.28}$	$-11.62^{+0.24}_{-2.76}$	$0.40^{+0.30}_{-0.20}$	$1.09^{+0.05}_{-0.03}$	$1.77^{+0.05}_{-0.05}$	1.4 ± 0.5	3.8 ± 1.1

Table 5
Analog Galaxy Parameters for Composite SEDs at $2.5 < z < 4.0$

Composite ID	Class	$\log_{10}(M/M_\odot)$	sSFR (yr^{-1})	A_V (mag)	(V–J)	(U–V)	r_e (kpc)	n
0	ELG	$8.59^{+0.63}_{-0.33}$	$-6.87^{+0.15}_{-1.51}$	$0.70^{+0.11}_{-0.70}$	$-0.36^{+0.38}_{-0.24}$	$0.35^{+0.19}_{-0.25}$	1.1 ± 0.5	1.5 ± 1.2
1	ELG	$8.84^{+0.49}_{-0.24}$	$-7.13^{+0.10}_{-1.25}$	$0.60^{+0.10}_{-0.50}$	$-0.18^{+0.35}_{-0.34}$	$0.24^{+0.17}_{-0.09}$	1.2 ± 0.5	1.3 ± 0.8
2	SFG	$9.30^{+0.23}_{-0.43}$	$-8.45^{+1.25}_{-0.33}$	$0.15^{+0.43}_{-0.15}$	$-0.07^{+0.30}_{-0.30}$	$0.23^{+0.08}_{-0.05}$	1.5 ± 0.4	1.6 ± 0.9
3	ELG	$8.84^{+0.26}_{-0.27}$	$-7.06^{+0.09}_{-0.08}$	$0.90^{+0.10}_{-0.10}$	$-0.10^{+0.16}_{-0.25}$	$0.35^{+0.23}_{-0.07}$	1.5 ± 0.6	1.2 ± 0.8
4	SFG	$9.43^{+0.30}_{-0.54}$	$-8.30^{+1.10}_{-0.60}$	$0.30^{+0.50}_{-0.30}$	$0.06^{+0.30}_{-0.17}$	$0.30^{+0.11}_{-0.10}$	1.6 ± 0.6	1.5 ± 0.7
5	SFG	$9.64^{+0.19}_{-0.29}$	$-8.99^{+0.46}_{-0.18}$	$0.20^{+0.20}_{-0.20}$	$0.11^{+0.21}_{-0.23}$	$0.35^{+0.16}_{-0.11}$	1.6 ± 0.7	1.1 ± 0.5
6	SFG	$9.12^{+0.72}_{-0.35}$	$-7.24^{+0.09}_{-1.71}$	$0.80^{+0.20}_{-0.70}$	$0.06^{+0.32}_{-0.31}$	$0.36^{+0.12}_{-0.09}$	1.7 ± 0.5	1.0 ± 0.6
7	SFG	$9.76^{+0.19}_{-0.24}$	$-9.00^{+0.36}_{-0.36}$	$0.30^{+0.32}_{-0.30}$	$0.21^{+0.30}_{-0.13}$	$0.55^{+0.09}_{-0.16}$	1.7 ± 0.6	1.9 ± 1.0
8	SFG	$9.72^{+0.24}_{-0.31}$	$-8.99^{+0.64}_{-0.37}$	$0.30^{+0.30}_{-0.20}$	$0.22^{+0.25}_{-0.23}$	$0.41^{+0.14}_{-0.10}$	1.7 ± 0.5	1.2 ± 0.6
9	SFG	$9.97^{+0.25}_{-0.31}$	$-8.82^{+0.29}_{-0.21}$	$0.60^{+0.28}_{-0.10}$	$0.58^{+0.28}_{-0.20}$	$0.62^{+0.11}_{-0.08}$	2.1 ± 0.8	1.1 ± 0.8
10	SFG	$9.83^{+0.26}_{-0.16}$	$-9.00^{+0.21}_{-0.44}$	$0.40^{+0.20}_{-0.30}$	$0.30^{+0.20}_{-0.19}$	$0.51^{+0.13}_{-0.12}$	1.8 ± 0.7	1.3 ± 0.7
11	SFG	$10.02^{+0.25}_{-0.27}$	$-9.00^{+0.19}_{-0.44}$	$0.50^{+0.30}_{-0.20}$	$0.42^{+0.21}_{-0.16}$	$0.62^{+0.10}_{-0.14}$	2.0 ± 0.6	1.4 ± 0.8
12	SFG	$10.23^{+0.27}_{-0.20}$	$-8.87^{+0.22}_{-0.20}$	$1.00^{+0.10}_{-0.10}$	$0.76^{+0.22}_{-0.04}$	$0.83^{+0.09}_{-0.11}$	2.2 ± 1.1	1.1 ± 0.3
13	SFG	$10.08^{+0.23}_{-0.26}$	$-9.07^{+0.41}_{-0.52}$	$0.70^{+0.20}_{-0.30}$	$0.54^{+0.21}_{-0.28}$	$0.65^{+0.16}_{-0.17}$	2.1 ± 0.6	1.5 ± 0.5
14	SFG	$10.05^{+0.22}_{-0.26}$	$-9.44^{+0.45}_{-0.55}$	$0.70^{+0.29}_{-0.30}$	$0.49^{+0.20}_{-0.30}$	$0.70^{+0.07}_{-0.15}$	2.8 ± 1.1	1.1 ± 0.4
15	SFG	$9.99^{+0.30}_{-0.26}$	$-9.61^{+0.58}_{-1.56}$	$0.80^{+0.10}_{-0.20}$	$0.55^{+0.12}_{-0.20}$	$0.84^{+0.04}_{-0.19}$	1.8 ± 0.8	1.1 ± 0.6
16	SFG	$10.96^{+0.20}_{-0.50}$	$-9.74^{+1.30}_{-0.40}$	$2.50^{+0.22}_{-0.41}$	$1.91^{+0.27}_{-0.11}$	$1.64^{+0.31}_{-0.30}$	2.8 ± 1.2	0.9 ± 0.4
17	SFG	$10.53^{+0.23}_{-0.41}$	$-9.07^{+0.55}_{-0.89}$	$1.50^{+0.34}_{-0.20}$	$1.30^{+0.33}_{-0.15}$	$1.15^{+0.16}_{-0.15}$	2.8 ± 0.7	1.2 ± 0.9
18	PSB	$10.50^{+0.39}_{-0.33}$	$-10.36^{+0.31}_{-0.69}$	$0.40^{+0.46}_{-0.30}$	$0.78^{+0.07}_{-0.35}$	$1.40^{+0.09}_{-0.05}$	1.1 ± 0.7	7.8 ± 0.2
19	PSB	$10.66^{+0.34}_{-0.20}$	$-11.66^{+0.96}_{-2.64}$	$0.50^{+0.30}_{-0.10}$	$0.89^{+0.21}_{-0.18}$	$1.59^{+0.22}_{-0.09}$	0.9 ± 0.4	3.1 ± 1.2

Finally, plots of the composite SEDs are shown in scaled F_λ-wavelength, all labeled with a composite ID number. For most of the composite SEDs, these are shown in individual panels, colored and separated into their classes as described in the text.

The exception to this is the SFGs at $1 < z < 3$, which are three to a panel. Composite SEDs are ordered by UV slope and are shown in Figures 13 and 14 (ELGs), Figures 15 and 16 (SFGs), Figure 17 (TGs), Figures 18 and 19 (PSBs), and Figure 20 (QGs).
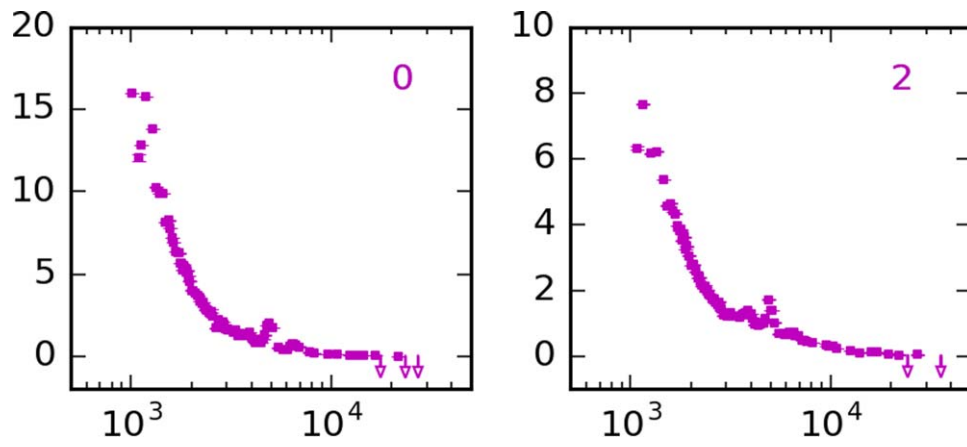
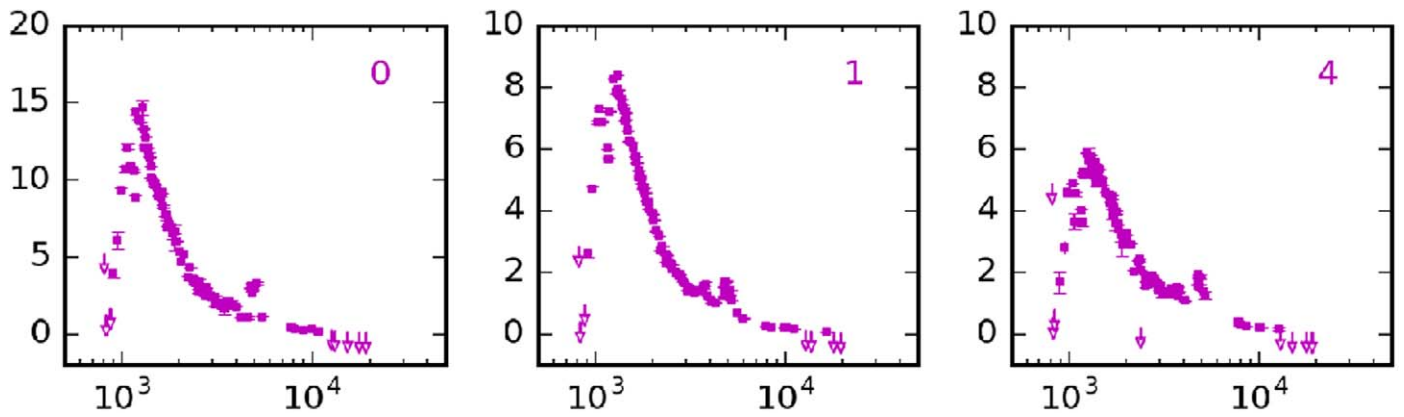**Figure 13.** Set of ELG composite SEDs from $1 < z < 3$ as scaled F_λ against wavelength.

Figure 14. Set of ELG composite SEDs from $2.5 < z < 4$ as scaled F_λ against wavelength.
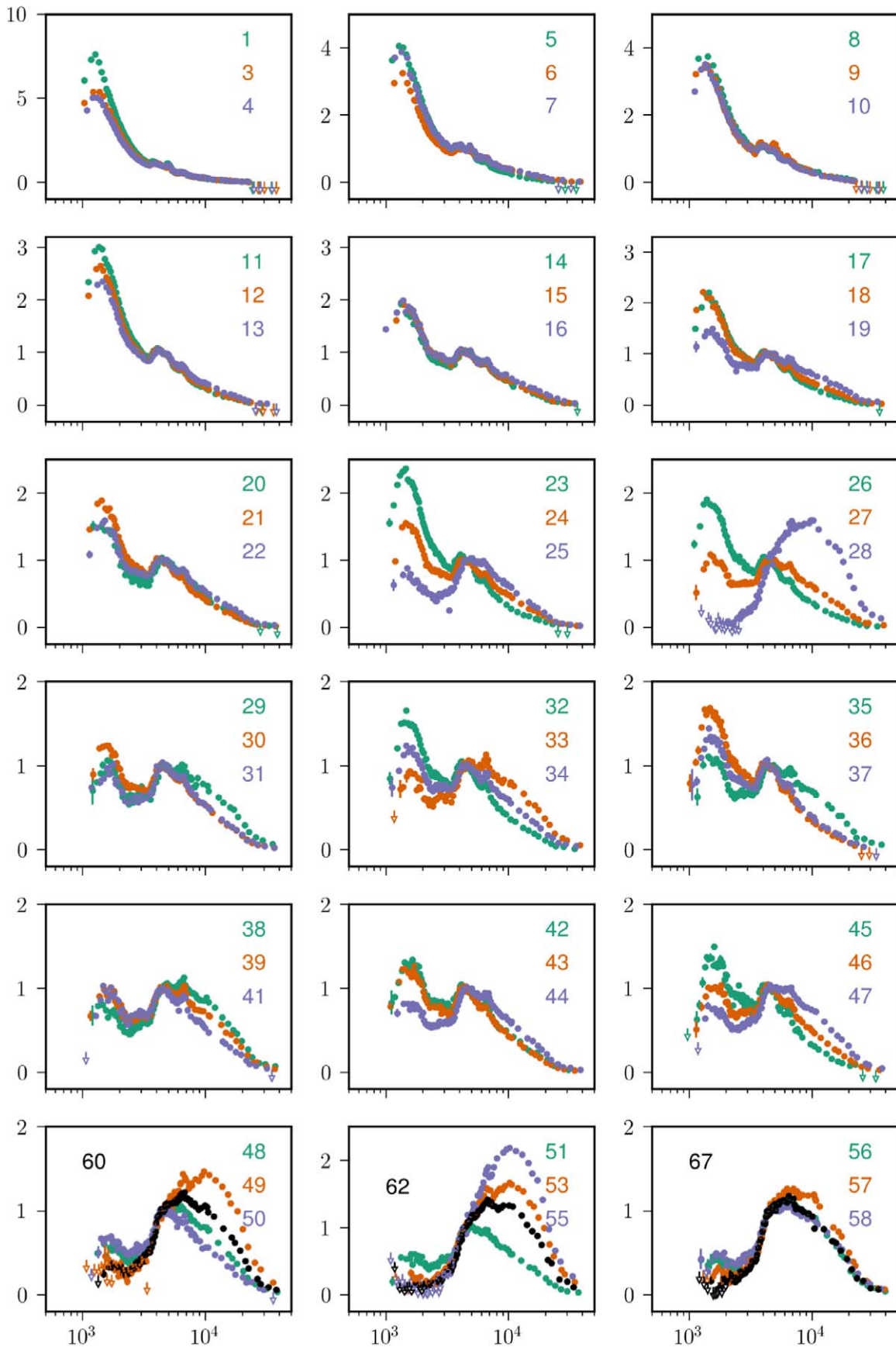
Figure 15. Set of SFG composite SEDs from $1 < z < 3$ as scaled F_λ against wavelength. Each panel has three composite SEDs—we have changed the blue color used throughout much of the paper for clarity and grouped by UV flux. Note that the y-axis range changes between panels, although the abscissae are identical. There are many composite SED pairs that are similar, and we do not claim that these are all separate populations, although many have differences, as shown throughout this work.
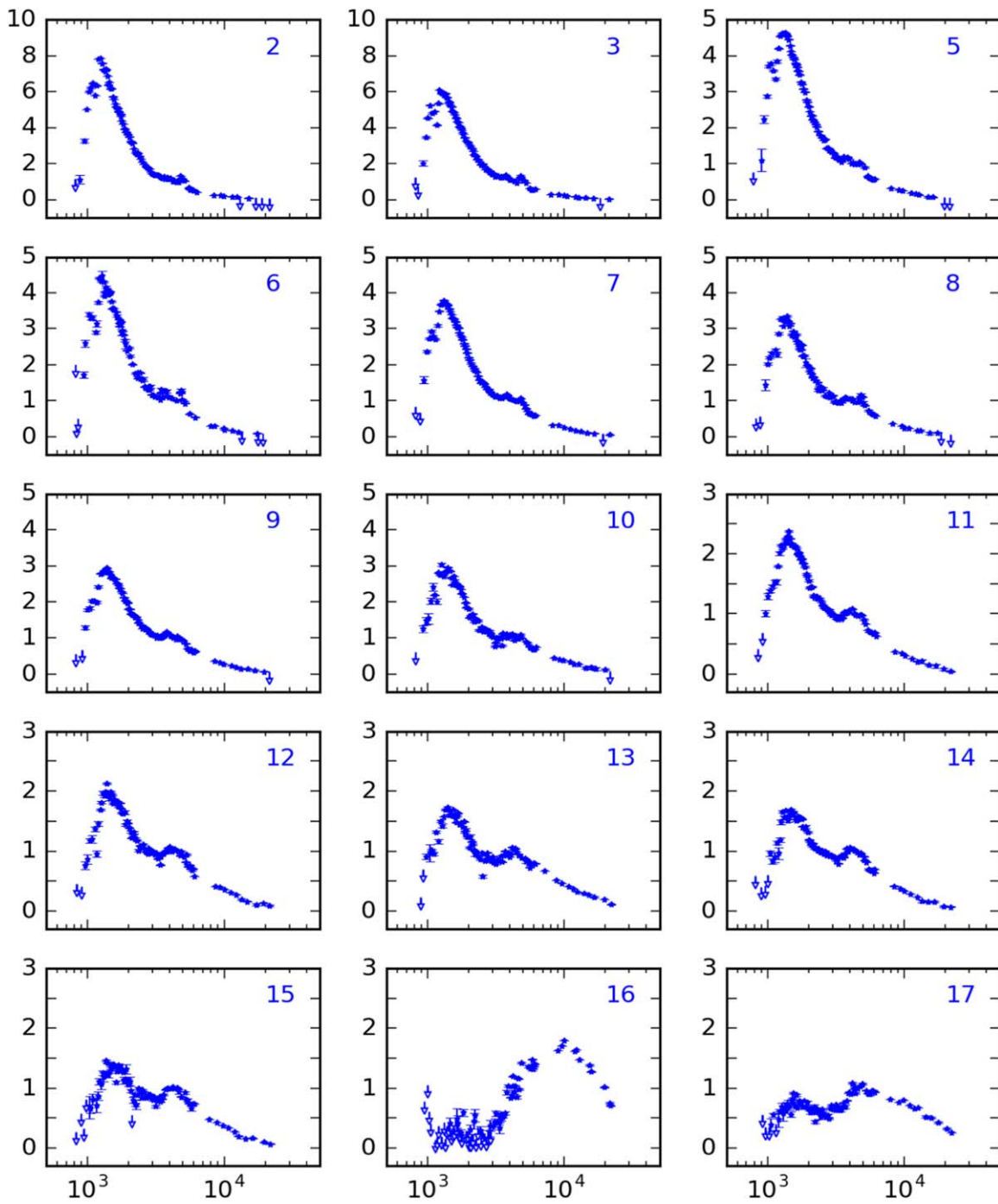
Figure 16. Set of SFG composite SEDs from $2.5 < z < 4$ as scaled F_λ against wavelength. Note that the y-axis range changes between panels, although the abscissae are identical.
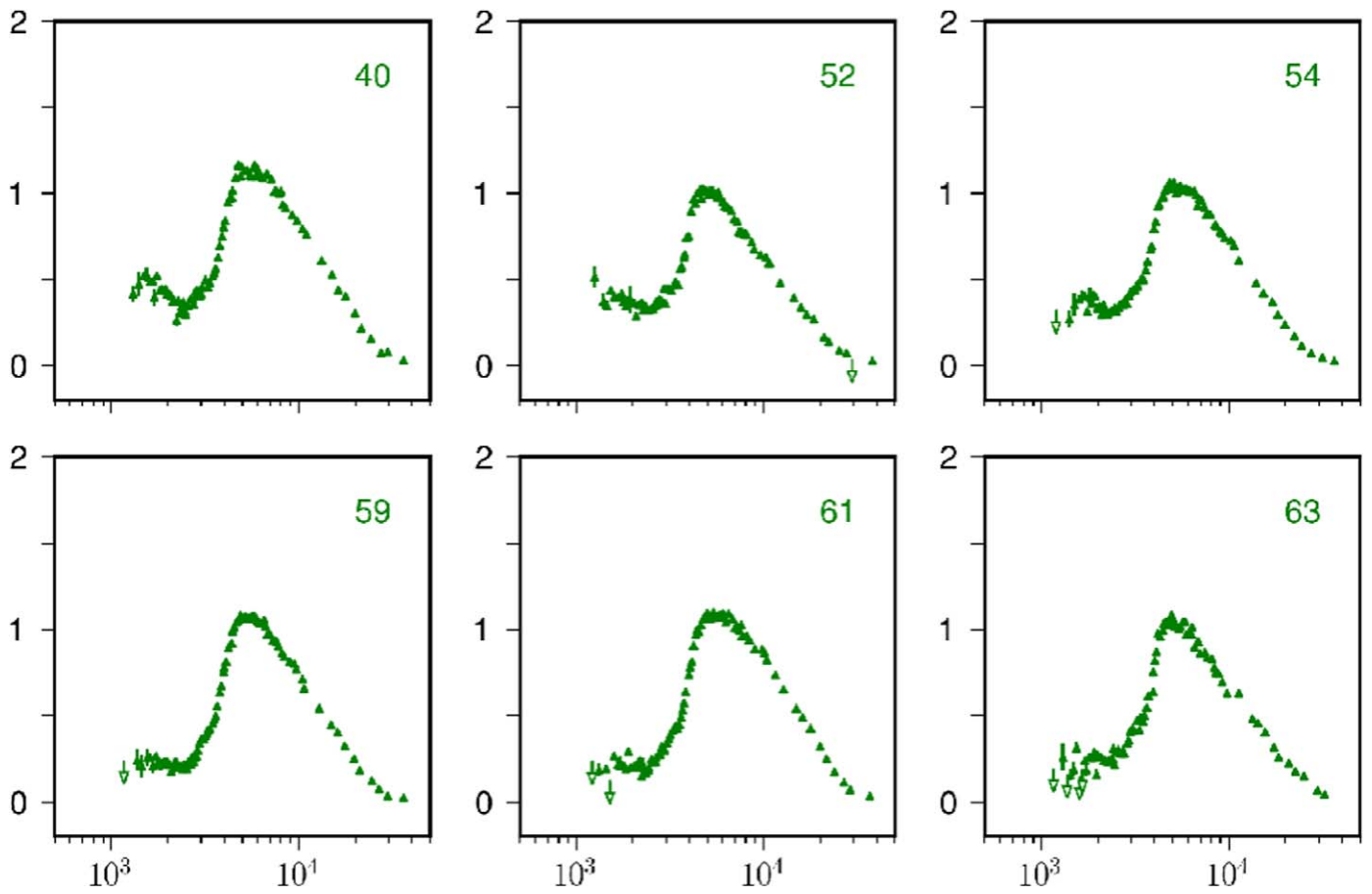
Figure 17. Set of TG composite SEDs from $1 < z < 3$ as scaled F_λ against wavelength.
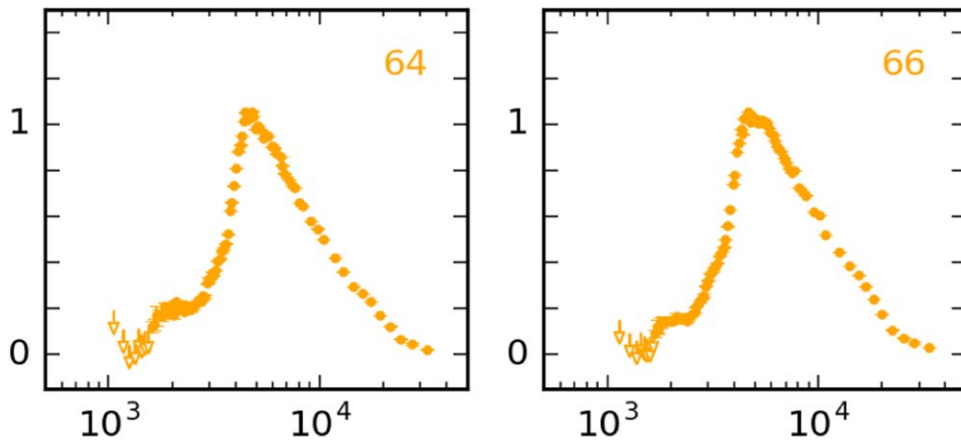
Figure 18. Set of PSB composite SEDs from $1 < z < 3$ as scaled F_λ against wavelength.
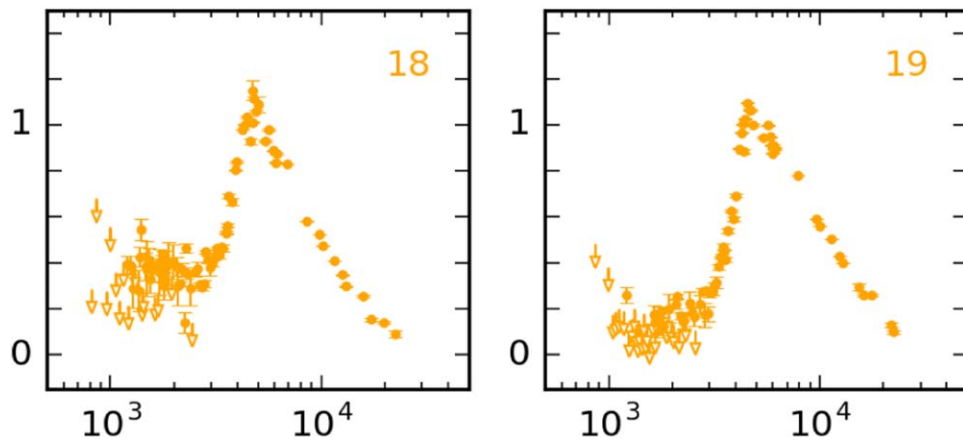
Figure 19. Set of PSB composite SEDs from $2.5 < z < 4$ as scaled F_λ against wavelength.
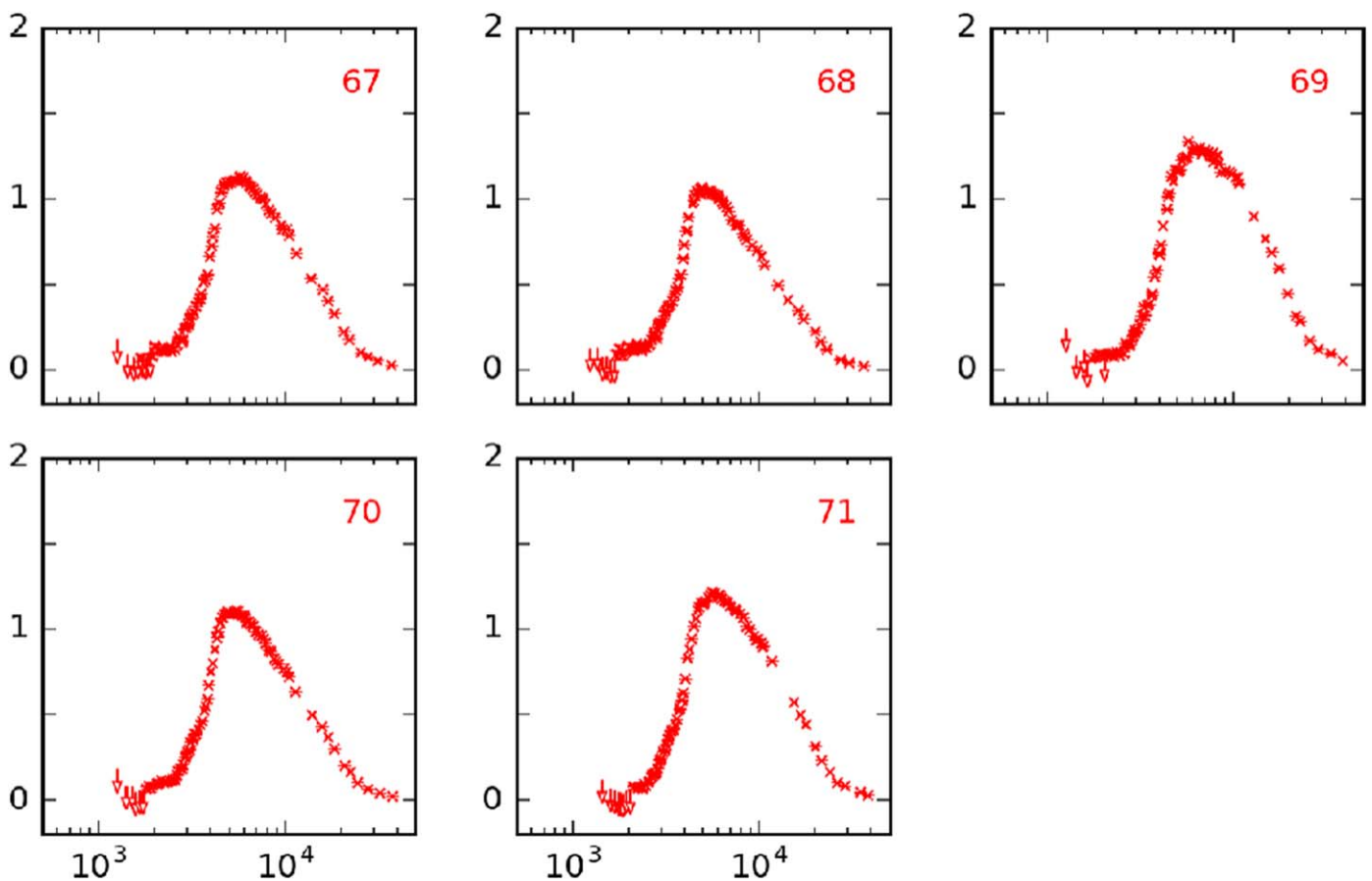
Figure 20. Set of QG composite SEDs from $1 < z < 3$ as scaled F_λ against wavelength.

ORCID iDs

Ben Forrest https://orcid.org/0000-0001-6003-0541
Kim-Vy H. Tran https://orcid.org/0000-0001-9208-2143
Jonathan H. Cohn https://orcid.org/0000-0003-1420-6037
Casey Papovich https://orcid.org/0000-0001-7503-8482
Rebecca Allen https://orcid.org/0000-0002-7278-9528
Michael Cowley https://orcid.org/0000-0002-4653-8637
Karl Glazebrook https://orcid.org/0000-0002-3254-9044
Lalitwadee Kawinwanichakij https://orcid.org/0000-0003-4032-2445
Themiya Nanayakkara https://orcid.org/0000-0003-2804-0648

Brett Salmon https://orcid.org/0000-0002-7453-7279
Lee R. Spitler https://orcid.org/0000-0001-5185-9876
Caroline M. S. Straatman https://orcid.org/0000-0001-5937-4590

References

Abazajian, K., Adelman-McCarthy, J. K., Ageros, M. A., et al. 2003, AJ, 126, 2081
Allen, R. J., Kacprzak, G. G., Glazebrook, K., et al. 2017, ApJL, 834, L11
Almaini, O., Wild, V., Maltby, D. T., et al. 2017, MNRAS, 472, 1401
The Astropy Collaboration, Robitaille, T. P., Tollerud, E. J., et al. 2013, A&A, 558, A33

Baldwin, J. A., Phillips, M. M., & Terlevich, R. 1981, PASP, 93, 5
Barro, G., Faber, S. M., Pérez-González, P. G., et al. 2013, ApJ, 765, 104
Behroozi, P. S., Wechsler, R. H., & Conroy, C. 2013, ApJ, 770, 57
Brammer, G. B., Sánchez-Janssen, R., Labbé, I., et al. 2012, ApJL, 758, L17
Brammer, G. B., van Dokkum, P. G., & Coppi, P. 2008, ApJ, 686, 1503
Brammer, G. B., Whitaker, K. E., van Dokkum, P. G., et al. 2009, ApJL, 706, L173
Brammer, G. B., Whitaker, K. E., van Dokkum, P. G., et al. 2011, ApJ, 739, 24
Brinchmann, J., Kunth, D., & Durret, F. 2008, A&A, 485, 657
Bruzual, A. G. 1983, ApJ, 273, 105
Bruzual, G., & Charlot, S. 2003, MNRAS, 344, 1000
Byler, N., Dalcanton, J., Conroy, C., et al. 2018, ApJ, 863, 14
Byler, N., Dalcanton, J. J., Conroy, C., & Johnson, B. D. 2017, ApJ, 840, 44
Capak, P., Cowie, L. L., Hu, E. M., et al. 2004, AJ, 127, 180
Cardamone, C. N., van Dokkum, P. G., Urry, C. M., et al. 2010, ApJS, 189, 270
Cassarà, L. P., Maccagni, D., Garilli, B., et al. 2016, A&A, 593, A9
Castellano, M., Sommariva, V., Fontana, A., et al. 2014, A&A, 566, A19
Chabrier, G. 2003, PASP, 115, 763
Ciesla, L., Elbaz, D., & Fensch, J. 2017, A&A, 608, A41
Couch, W. J., & Sharples, R. M. 1987, MNRAS, 229, 423
Cowie, L. L., & Hu, E. M. 1998, AJ, 115, 1319
Cowley, M. J., Spitler, L. R., Tran, K.-V. H., et al. 2016, MNRAS, 457, 629
Darvish, B., Mobasher, B., Sobral, D., et al. 2016, ApJ, 825, 113
Davé, R., Rafieferantsoa, M. H., & Thompson, R. J. 2017, MNRAS, 471, 1671
Dekel, A., & Burkert, A. 2014, MNRAS, 438, 1870
Dressler, A., & Gunn, J. E. 1983, ApJ, 270, 7
Dressler, A., Kelson, D. D., & Abramson, L. E. 2018, arXiv:1805.04110
Eales, S., de Vis, P. W. L., Smith, M., et al. 2017, MNRAS, 465, 3125
Eales, S., Smith, D., Bourne, N., et al. 2018, MNRAS, 473, 3507
Elbaz, D., Dickinson, M., Hwang, H. S., et al. 2011, A&A, 533, A119
Erb, D. K., Pettini, M., Shapley, A. E., et al. 2010, ApJ, 719, 1168
Erben, T., Hildebrandt, H., Lerchster, M., et al. 2009, A&A, 493, 1197
Erben, T., Schirmer, M., Dietrich, J. P., et al. 2005, AN, 326, 432
Faisst, A. L., Carollo, C. M., Capak, P. L., et al. 2017, ApJ, 839, 71
Fang, J. J., Faber, S. M., Koo, D. C., et al. 2018, ApJ, 858, 100
Fang, J. J., Faber, S. M., Koo, D. C., & Dekel, A. 2013, ApJ, 776, 63
Fang, J. J., Faber, S. M., Salim, S., Graves, G. J., & Rich, R. M. 2012, ApJ, 761, 23
Ferland, G. J., Korista, K. T., Verner, D. A., et al. 1998, PASP, 110, 761
Finkelstein, S. L., Papovich, C., Dickinson, M., et al. 2013, Natur, 502, 524
Fioc, M., & Rocca-Volmerange, B. 1999, 18, arXiv:astro-ph/9912179
Foltz, R., Wilson, G., Muzzin, A., et al. 2018, arXiv:1803.03305
Fontana, A., Dunlop, J. S., Paris, D., et al. 2014, A&A, 570, A11
Forrest, B., Tran, K.-V. H., Broussard, A., et al. 2017, ApJL, 838, L12
Forrest, B., Tran, K.-V. H., Tomczak, A. R., et al. 2016, ApJL, 818, L26
Fumagalli, M., Patel, S. G., Franx, M., et al. 2012, ApJL, 757, L22
Furusawa, H., Kosugi, G., Akiyama, M., et al. 2008, ApJS, 176, 1
Geach, J. E., Smail, I., Best, P. N., et al. 2008, MNRAS, 388, 1473
Giacconi, R., Zirm, A., Wang, J., et al. 2002, ApJS, 139, 369
Giavalisco, M., Ferguson, H. C., Koekemoer, A. M., et al. 2004, ApJL, 600, L93
Glazebrook, K., Schreiber, C., Labbé, I., et al. 2017, Natur, 544, 71
Grogin, N. A., Kocevski, D. D., Faber, S. M., et al. 2011, ApJS, 197, 35
Hildebrandt, H., Erben, T., Dietrich, J. P., et al. 2006, A&A, 452, 1121
Hildebrandt, H., Pielorz, J., Erben, T., et al. 2009, A&A, 498, 725
Hsieh, B.-C., Wang, W.-H., Hsieh, C.-C., et al. 2012, ApJS, 203, 23
Hu, E. M., & McMahon, R. G. 1996, Natur, 382, 231
Inoue, A. K. 2011, MNRAS, 415, 2920
Izotov, Y. I., Guseva, N. G., Fricke, K. J., & Henkel, C. 2016, MNRAS, 462, 4427
Kauffmann, G., Heckman, T. M., White, S. D. M., et al. 2003, MNRAS, 341, 54
Kawinwanichakij, L., Papovich, C., Quadri, R. F., et al. 2017, ApJ, 847, 134
Kennicutt, R. C., & Evans, N. J. 2012, ARA&A, 50, 531
Kewley, L. J., Dopita, M. A., Leitherer, C., et al. 2013, ApJ, 774, 100
Khostovan, A. A., Sobral, D., Mobasher, B., et al. 2016, MNRAS, 463, 2363
Koekemoer, A. M., Faber, S. M., Ferguson, H. C., et al. 2011, ApJS, 197, 36
Kriek, M., & Conroy, C. 2013, ApJL, 775, L16
Kriek, M., van Dokkum, P. G., Labbé, I., et al. 2009, ApJ, 700, 221
Kriek, M., van Dokkum, P. G., Whitaker, K. E., et al. 2011, ApJ, 743, 168
Labbé, I., Huang, J., Franx, M., et al. 2005, ApJL, 624, L81
Labbé, I., Oesch, P. a., Bouwens, R. J., et al. 2013, ApJL, 777, L19
Lawrence, a., Warren, S. J., Almaini, O., et al. 2007, MNRAS, 379, 1599
Leja, J., Johnson, B. D., Conroy, C., van Dokkum, P. G., & Byler, N. 2017, ApJ, 837, 170
Maltby, D. T., Almaini, O., Wild, V., et al. 2016, MNRAS, 459, L114
Martig, M., Bournaud, F., Teyssier, R., & Dekel, A. 2009, ApJ, 707, 250
Martin, D. C., Small, T., Schiminovich, D., et al. 2007, ApJS, 173, 415
McCracken, H. J., Milvang-Jensen, B., Dunlop, J., et al. 2012, A&A, 544, A156
Mendez, A. J., Coil, A. L., Lotz, J., et al. 2011, ApJ, 736, 110
Miller, A. S., & Coe, M. J. 1996, MNRAS, 279, 293
Nakajima, K., & Ouchi, M. 2014, MNRAS, 442, 900
Nanayakkara, T., Glazebrook, K., Kacprzak, G. G., et al. 2016, ApJ, 828, 21
Nelson, D., Pillepich, A., Springel, V., et al. 2018, MNRAS, 475, 624
Nonino, M., Dickinson, M., Rosati, P., et al. 2009, ApJS, 183, 244
Pacifici, C., Kassin, S. A., Weiner, B. J., et al. 2016, ApJ, 832, 79
Pandya, V., Brennan, R., Somerville, R. S., et al. 2017, MNRAS, 472, 2054
Papovich, C., Dickinson, M., & Ferguson, H. C. 2001, ApJ, 559, 620
Papovich, C., Kawinwanichakij, L., Quadri, R., et al. 2018, ApJ, 854, 30
Papovich, C., Labbé, I., Quadri, R., et al. 2015, ApJ, 803, 26
Patel, S. G., Holden, B. P., Kelson, D. D., et al. 2012, ApJL, 748, L27
Peng, Y.-j., Lilly, S. J., Kovač, K., et al. 2010, ApJ, 721, 193
Persson, S. E., Murphy, D. C., Smee, S., et al. 2013, PASP, 125, 654
Poggianti, B. M., Aragón-Salamanca, A., Zaritsky, D., et al. 2009, ApJ, 693, 112
Poggianti, B. M., & Barbaro, G. 1997, A&A, 325, 1025
Rampazzo, R., Marino, A., Tantalo, R., et al. 2007, MNRAS, 381, 245
Retzlaff, J., Rosati, P., Dickinson, M., et al. 2010, A&A, 511, A50
Rowlands, K., Wild, V., Bourne, N., et al. 2018, MNRAS, 473, 1168
Salim, S., Rich, R. M., Charlot, S., et al. 2007, ApJS, 173, 267
Salmon, B., Papovich, C., Finkelstein, S. L., et al. 2015, ApJ, 799, 183
Schawinski, K., Urry, C. M., Simmons, B. D., et al. 2014, MNRAS, 440, 889
Schiminovich, D., Wyder, T. K., Martin, D. C., et al. 2007, ApJS, 173, 315
Scoville, N., Aussel, H., Brusa, M., et al. 2007, ApJS, 172, 1
Shapley, a. E., Steidel, C. C., Pettini, M., & Adelberger, K. L. 2003, ApJ, 588, 65
Smit, R., Bouwens, R. J., Labbé, I., et al. 2014, ApJ, 784, 58
Smit, R., Bouwens, R. J., Labbé, I., et al. 2015, ApJ, 801, 122
Sobral, D., Smail, I., Best, P. N., et al. 2013, MNRAS, 428, 1128
Sparre, M., Hayward, C. C., Springel, V., et al. 2015, MNRAS, 447, 3548
Spitler, L. R., Straatman, C. M. S., Labbé, I., et al. 2014, ApJL, 787, L36
Stark, D. P., Schenker, M. a., Ellis, R., et al. 2013, ApJ, 763, 129
Straatman, C. M. S., Spitler, L. R., Quadri, R. F., et al. 2016, ApJ, 830, 51
Tacchella, S., Dekel, A., Carollo, C. M., et al. 2016, MNRAS, 457, 2790
Taniguchi, Y., Scoville, N., Murayama, T., et al. 2007, ApJS, 172, 9
Teplitz, H. I., Malkan, M. a., & McLean, I. S. 1999, ApJ, 514, 33
Tomczak, A. R., Quadri, R. F., Tran, K.-v. H., et al. 2016, ApJ, 817, 118
Tran, K.-V. H., Franx, M., Illingworth, G., Kelson, D. D., & van Dokkum, P. 2003, ApJ, 599, 865
Tran, K.-v. H., Franx, M., Illingworth, G. D., et al. 2004, ApJ, 609, 683
Trayford, J. W., Theuns, T., Bower, R. G., et al. 2016, MNRAS, 460, 3925
van der Wel, A., Bell, E. F., Häussler, B., et al. 2012, ApJS, 203, 24
van Dokkum, P. G., Brammer, G., Fumagalli, M., et al. 2011, ApJL, 743, L15
van Dokkum, P. G., Labbé, I., Marchesini, D., et al. 2009, PASP, 121, 2
Vanderplas, J., & Connolly, A. 2009, AJ, 138, 1365
Whitaker, K. E., Kriek, M., van Dokkum, P. G., et al. 2012a, ApJ, 745, 179
Whitaker, K. E., Labbé, I., van Dokkum, P. G., et al. 2011, ApJ, 735, 86
Whitaker, K. E., van Dokkum, P. G., Brammer, G., & Franx, M. 2012b, ApJL, 754, L29
Wild, V., Almaini, O., Cirasuolo, M., et al. 2014, MNRAS, 440, 1880
Wild, V., Almaini, O., Dunlop, J., et al. 2016, MNRAS, 463, 832
Wilkinson, C. L., Pimbblet, K. A., & Stott, J. P. 2017, MNRAS, 472, 1447
Williams, R. J., Quadri, R. F., Franx, M., van Dokkum, P., & Labbé, I. 2009, ApJ, 691, 1879
Windhorst, R. A., Cohen, S. H., Hathi, N. P., et al. 2011, ApJS, 193, 27
Wittman, D. M., Tyson, J. A., Dell'Antonio, I. P., et al. 2002, Proc. SPIE, 4836, 73
Wuyts, S., Labbé, I., Förster Schreiber, N. M., et al. 2008, ApJ, 682, 985
Wuyts, S., Labbe, I., Franx, M., et al. 2007, ApJ, 655, 51
Wyder, T. K., Martin, D. C., Schiminovich, D., et al. 2007, ApJS, 173, 293
Zolotov, A., Dekel, A., Mandelker, N., et al. 2015, MNRAS, 450, 2327